JOURNAL OF GEOPHYSICAL RESEARCH, VOL. ???, XXXX, DOI:10.1029/,

Crustal shear velocity structure of the western US inferred from ambient seismic noise and earthquake data

M. P. Moschetti,[1] M. H. Ritzwoller,[1] F.-C. Lin,[1] Y. Yang[1]

F.-C. Lin, Center for Imaging the Earth's Interior, Department of Physics, University of Colorado, 390 UCB, Boulder, CO, 80390-0390, USA. (fan-chi.lin@colorado.edu)

M. P. Moschetti, Center for Imaging the Earth's Interior, Department of Physics, University of Colorado, 390 UCB, Boulder, CO, 80390-0390, USA. (morganm@ciei.colorado.edu)

M. H. Ritzwoller, Center for Imaging the Earth's Interior, Department of Physics, University of Colorado, 390 UCB, Boulder, CO, 80390-0390, USA. (michael.ritzwoller@colorado.edu)

Y. Yang, Center for Imaging the Earth's Interior, Department of Physics, University of Colorado, 390 UCB, Boulder, CO, 80390-0390, USA. (yingjie.yang@colorado.edu)

[1]Center for Imaging the Earth's Interior,
Department of Physics, University of
Colorado, Boulder, CO, USA.

Abstract. Surface wave dispersion measurements from ambient seismic noise and array-based measurements from teleseismic earthquakes observed on the USArray Transportable Array are inverted using a Monte Carlo method for a 3-D V_S model of the crust and uppermost mantle beneath the western United States. The combination of data from these methods produces exceptionally broad-band dispersion information from 6 to 100 sec period, which constrains shear velocity structures in the crust and uppermost mantle to a depth of more than 100 km. The high lateral resolution produced by the TA data and the broad-bandedness of the dispersion information motivate the question of the appropriate parameterization for a 3-D model, particularly for the crustal part of the model. We show that a relatively simple model in which V_S increases monotonically with depth in the crust can fit the data well across more than 90% of the study region, except in eight discrete areas where greater crustal complexity apparently exists. The regions of exceptional crustal complexity are the Olympic Peninsula, the Yakima Fold Belt, the southern Cascadia Forearc, the Great Valley of California, the Salton Trough, the northwestern Basin and Range, the Snake River Plain, and the Wasatch Mountains. We also show that a strong Rayleigh-Love discrepancy exists across much of the western US, which can be resolved by introducing radial anisotropy in both the mantle and notably the crust. Analysis is focused on demonstrating the existence of the crustal radial anisotropy and discussion concentrates on the crustal part of the isotropic model that results from the radially anisotropic model by Voigt averaging. Model uncer-

tainties from the Monte Carlo inversion are used to identify robust isotropic features in the model.

1. Introduction

Although numerous seismological studies have investigated the velocity structure of the crust and upper mantle beneath the western United States (US) on multiple spatial scales [e.g., *Grand*, 1994; *Fuis et al.*, 2001; *Shapiro and Ritzwoller*, 2002; *Tanimoto and Sheldrake*, 2002; *Gilbert and Sheehan*, 2004; *van der Lee and Frederiksen*, 2005; *Ramachandran et al.*, 2006; *Marone et al.*, 2007; *Yan and Clayton*, 2007; *Nettles and Dziewonski*, 2008], the construction of crustal velocity models over extended regions has been limited by the insensitivity or relatively poor resolution of seismological techniques to crustal structure. Surface wave inversions, for example, can constrain crustal V_S across broad regions, but crustal imaging with surface waves is generally hindered by the complexity or absence of short period ($<$ 20 sec) dispersion measurements in earthquake signals. The development of ambient noise tomography (ANT) now permits crustal imaging across large regions by enabling the measurement of short period surface wave dispersion measurements between pairs of seismic stations. Theoretical investigations [*Snieder*, 2004; *Wapenaar*, 2004], experiments [*Lobkis and Weaver*, 2001; *Weaver and Lobkis*, 2001] and seismological applications [*Shapiro and Campillo*, 2004; *Sabra et al.*, 2005; *Shapiro et al.*, 2005] have shown that the cross-correlation of ambient seismic noise records from two seismic stations may be used to calculate the empirical Green's function (EGF), which contains information about seismic wave propagation between the stations. Surface wave dispersion measurements down to 6 sec are readily made on EGFs in the western US (e.g., *Moschetti et al.* [2007], *Lin et al.* [2008]) and provide strong constraints on crustal velocity structure. The inversion of inter-station dispersion measurements obtained from the EGFs to construct period-dependent dispersion maps is termed ANT and has already been used to produce dispersion maps across various regions around the globe and at multiple scales [e.g., *Yao et al.*, 2006; *Brenguier et al.*, 2007; *Cho et al.*, 2007; *Lin et al.*, 2007; *Villasenor et al.*, 2007; *Yang et al.*, 2007; *Bensen et al.*, 2008; *Yang et al.*, 2008a; *Zheng et al.*, 2008].

Knowledge of the seismic velocity structure beneath the western US has benefited from the application of novel observational techniques to data from the USArray Transportable Array (TA). As the TA moves across the US, about 400 stations on a nearly-uniform 70 km grid record continuous data simultaneously. Each seismic station collects data for about two years before it is redeployed to a new location. The station density and spatial coverage of the TA span the resolution gap between regional[e.g., *Tanimoto and Sheldrake*, 2002] and global-scale [e.g., *van der Lee and Frederiksen*, 2005; *Shapiro and Ritzwoller*, 2002] studies. Detailed images of the crust and upper mantle in the western US have begun to emerge [e.g., *Gilbert and Fouch*, 2007; *Burdick et al.*, 2008; *Pollitz*, 2008; *Yang et al.*, 2008b; *West et al.*, 2009].

In this study, we apply ANT together with multiple plane wave earthquake tomography(MPWT) [*Yang et al.*, 2008b] to data from the TA. Application of ANT to the TA data provides Rayleigh wave group [*Moschetti et al.*, 2007] and Rayleigh and Love wave phase speed [*Lin et al.*, 2008] maps, which are strongly sensitive to the crust and uppermost mantle and cover the entire western US. MPWT likewise benefits from the high station density and broad spatial coverage of the TA. MPWT is an extension of the two plane wave method of *Forsyth and Li* [2005] in which complexities in the incoming wave field are fit with two plane waves. While two plane waves are sufficient to characterize the incoming wave field for relatively small arrays, for regions the size of the western US additional plane waves are needed to model the incoming wave field from each earthquake. MPWT provides Rayleigh wave phase speed estimates across the western US that are at about the same resolution and are readily inverted together with the dispersion measurements from ANT [*Yang et al.*, 2008b].

It is common practice in seismology to invert dispersion maps from earthquake measurements [*Shapiro and Ritzwoller*, 2002] or ANT [*Cho et al.*, 2007; *Bensen et al.*, 2009; *Stehly et al.*, 2009], as well as to use them jointly [*Yao et al.*, 2007; *Yang et al.*, 2008a, b], to infer the 3-D V_S structure of the crust and upper mantle. Notably, *Bensen et al.* [2009] carried out an inversion of Rayleigh and Love wave dispersion measurements obtained from ANT for V_S structure across the entire US. However, this work was completed before the TA was deployed in the western US and the corresponding resolution is lower than what now can be achieved. *Yang et al.* [2008b] inverted Rayleigh wave phase speed measurements from ANT and MPWT for a V_{SV} model of the crust and upper mantle in the western US, but this study did not include Love waves and the model did not account for the crustal and uppermost mantle radial anisotropy ($V_{SH} \neq V_{S!V}$) that has been documented, for example, by *Nettles and Dziewonski* [2008], *Bensen et al.* [2009], and *Moschetti et al.* [2009]. Inversions of Rayleigh wave data alone cannot untangle shear-velocity perturbations caused by radial anisotropy from those caused by isotropic wave speed anomalies. In addition to Love and Rayleigh wave phase speed measurements, we incorporate here Rayleigh wave group speed data from ANT. Group speed measurements have shallower depth sensitivity than phase speed measurements at the same period and provide additional constraints on crustal velocity structure.

We seek here, in particular, to identify a single parameterization, particularly of the crust, that can be applied across the entire western US except perhaps at isolated locations of greater complexity. We document how across most of the western US crustal wave speeds can be considered to increase monotonically with depth (thus crustal low velocity zones generally are not required by the data), but crustal and upper mantle radial anisotropy is needed to fit Rayleigh and Love wave dispersion data simultaneously. Our discussion is focused, however, on the isotropic component of the 3-D radially anisotropic V_S model. The isotropic model presented here is constructed by Voigt averaging the V_{SH} and V_{SV} models that result from the radially anisotropic inversion. Discussion and interpretation of the radial anisotropy is the subject of *Moschetti et al.* [2009].

2. Methods

The inversion of surface wave dispersion measurements for a 3-D V_S model is carried out in two steps. The first step, termed surface wave tomography, is the inversion for Rayleigh and Love wave dispersion maps. This step is described by *Moschetti et al.* [2007], *Lin et al.* [2008], and *Yang et al.* [2008b]. The second step, which we carry out here, is inversion of the surface wave dispersion maps for a 3-D V_S model. Here, we use a Monte Carlo method to infer a radially anisotropic V_S model of the crust and uppermost mantle beneath the western US, referred to as model m_1. We calculate the isotropic component of this model by Voigt averaging. For comparison, we also carry out the direct inversion for an isotropic model called m_0. Because we employ a Monte Carlo inversion scheme, the V_S structure beneath each grid point is represented by a set of models that fit the data similarly well, which provides uncertainty estimates used to identify robust model features.

2.1. Surface wave tomography and construction of local dispersion curves

Surface wave dispersion measurements from ANT and MPWT are combined because the joint period band is broader than the individual bands. ANT provides short- to intermediate-period measurements (6 – 40 sec) and MPWT provides intermediate- to long-period measurements (25 – 100 sec). The combined dispersion curve at each location has strong sensitivity to both the crust and upper mantle. The dispersion maps and measurements of *Moschetti et al.* [2007], *Yang et al.* [2008b] and *Lin et al.* [2008] are extended in this study. We briefly summarize these methods here.

2.1.1. Surface wave tomography

Ambient noise data processing entails station record pre-processing (filtering, time and frequency domain normalization), cross-correlation of station records to produce empirical Green's functions (EGFs), selection of EGFs, measurement of group and phase speeds, and inversion of the group and phase speed measurements at each period for dispersion maps. The methods described by *Bensen et al.* [2007] and *Lin et al.* [2008] are followed here. By cross-correlating seismic records observed at 526 stations between October 2004 and December 2007, more than 128,000 EGFs are calculated. Most of the waveform data is taken from TA stations, but additional data from regional networks is also incorporated. Fig. 1 presents the major physiographic provinces and the locations of seismic stations used in this study. Because of the evolving nature of the TA, not all of the stations operate concurrently. The resulting time series range from six months to more than three years in duration. Linear tomographic inversions of the inter-station Rayleigh wave group and phase speeds and the Love wave phase speeds are carried out using Gaussian-shaped sensitivity kernels centered on the great-circle path between stations [*Barmin et al.*, 2001].

The Rayleigh and Love wave dispersion maps that result are in period bands of 6 – 40 and 8 – 32 sec, respectively. Because of the large uncertainties associated with the Love wave group speeds, we do not incorporate these data in the inversion for V_S structure.

The ANT-derived dispersion maps are updated and expanded from the Rayleigh wave group speed maps presented by *Moschetti et al.* [2007] and the Rayleigh and Love wave phase speed maps of *Lin et al.* [2008]. The measurement of Rayleigh wave phase speeds from teleseismic earthquakes using MPWT follows the methods of *Yang et al.* [2008b]. Rayleigh wave phase speed maps are constructed using 250 earthquakes recorded by the TA between January 2006 and September 2008. Twelve independent plane waves are used to model the incoming wave field at the TA for each earthquake. Rayleigh wave phase speed maps from MPWT are generated in the 25 – 100 sec period band.

2.1.2. Local dispersion curves

To generate the local dispersion curves from the dispersion maps, at each 0.5° grid point group and phase speeds are selected as a function of period. Separate local dispersion curves are constructed from the dispersion maps obtained from ANT and MPWT. In the period band of overlap of the methods (25 – 40 sec), *Yang et al.* [2008b] demonstrated substantial agreement between the Rayleigh wave phase estimates. The mean absolute difference between the MPWT and ANT phase speed estimates in the 25 – 40 sec period band is about 15 m/s, which, as discussed below, is within a standard deviation of the dispersion measurements. (More recent work has further reduced this gap.) We follow *Yang et al.* [2008b] by averaging measurements in the overlapping period band to produce combined Rayleigh wave phase speed curves with a period band of 6 – 100 sec. These dispersion curves are sensitive to both crustal and upper mantle velocity structures.

Examples of the local dispersion curves are plotted in Fig. 2 and present some of the variation observed between the group and phase speeds from different regions. Although the focus of this study is the crustal structure of the western US, and dispersion measurements from ANT provide the strongest constraints at this depth, the incorporation of the MPWT measurements reduces the wave speed trade-off across the Moho and they provide improved constraints on upper mantle velocity structure. Love wave measurements have not yet been obtained with MPWT, so they derive entirely from ANT between 8 and 32 sec period. Love wave constraints on mantle structure, therefore, are much weaker than from Rayleigh waves.

2.1.3. Data uncertainties

We require uncertainty estimates for the local dispersion curves taken from the dispersion maps in order to assess the fit of model-predicted dispersion curves and to weight data in the inversion. Estimates of uncertainties in the inter-station ambient noise dispersion measurements are obtained in a straightforward way by temporal subsetting [e.g., *Bensen et al.*, 2007]. Estimates of local uncertainties for the dispersion maps are not as straightforward, although uncertainties in the Rayleigh wave phase speeds from ambient seismic noise are now directly calculated by Eikonal tomography [*Lin et al.*, 2009]. To estimate uncertainties in local Rayleigh wave group and Love wave phase dispersion curves we simply scale the Rayleigh wave phase uncertainties by the relative errors in the inter-station ambient noise dispersion measurements. Specifically, uncertainties in ambient noise dispersion measurements are determined in two steps. (1) We estimate the ratios of the measurement uncertainties of the Rayleigh wave group and Love wave phase speeds compared to the Rayleigh wave phase speeds (i.e., $\sigma^{RG}(T)/\sigma^{RP}(T)$ and $\sigma^{LP}(T)/\sigma^{RP}(T)$)

from the temporal variability in the observed EGFs. RP, RG and LP refer to Rayleigh wave phase and group speed and Love wave phase speed, respectively, and T is the period of the measurement. To calculate the temporal variations in the Rayleigh and Love wave inter-station dispersion measurements, we use 34 and 21 six-month time windows, respectively. These uncertainty ratios, averaged over the study region, are plotted in Fig. 3b. (2) We then use the uncertainty ratios of the measured data to scale the Rayleigh wave phase speed uncertainties ($\tilde{\sigma}_i^{RP}$) determined from Eikonal tomography. Examples of the Rayleigh wave phase speed uncertainties from Eikonal tomography, at several periods, are presented in Fig. 4. Eqns. (1) and (2) are used to estimate uncertainty values for the Rayleigh wave group speed and Love wave phase speed at each grid point, i.

$$\tilde{\sigma}_i^{RG}(T) = \frac{\sigma^{RG}(T)}{\sigma^{RP}(T)}\tilde{\sigma}_i^{RP}(T) \quad (1)$$

$$\tilde{\sigma}_i^{LP}(T) = \frac{\sigma^{LP}(T)}{\sigma^{RP}(T)}\tilde{\sigma}_i^{RP}(T) \quad (2)$$

Averages across the study region of the local uncertainties in the dispersion curves from the ambient noise are presented in Fig. 3c. Spatially- and frequency-averaged uncertainties in the Rayleigh wave phase and group speed and Love wave phase speed are 14.5, 36.8, and 13.4 m/s, respectively. Examples of the uncertainty values in the Rayleigh wave phase and group speeds and Love wave phase speeds from three geographic grid points are plotted as error bars in the dispersion curves of Fig. 2.

Uncertainties in the Rayleigh wave phase speed maps derived from MPWT follow the method of *Yang et al.* [2008b] in which estimates are calculated from the inversion residuals. Uncertainty values are plotted as a function of period in Fig. 3a and show a mean uncertainty value of 27.6 m/s. On average, Rayleigh wave phase speed uncertainty from

MPWT is estimated to be about twice the phase speed uncertainties from ambient noise, but less than the ambient noise group speed errors.

2.2. Inversion of local dispersion curves for a 3-D V_S model

The data for the V_S inversion are the local Rayleigh and Love wave dispersion curves generated on a 0.5°-by-0.5° grid across the study region. At each grid point we use a Monte Carlo method to sample parameter space for many trial models and assess the misfit of the corresponding predicted dispersion curves to the dispersion data. All models with corresponding data misfits less than a misfit threshold value are accepted and form the set of "acceptable models" at that grid point. This general inversion procedure has been used previously to construct regional- and global-scale V_S models [*Shapiro and Ritzwoller*, 2002; *Yang et al.*, 2008a; *Bensen et al.*, 2009]. From the set of accepted models at each grid point, we calculate the mean and standard deviation to represent the velocity structure and uncertainty as a function of depth.

For the purpose of comparison, we invert the local dispersion curves for two models. (1) We first invert the Rayleigh and Love wave data for an initial isotropic ($V_{SH} = V_{SV}$) model, m_0. This inversion also defines a restricted parameter space for each grid point to be used in the construction of the second model. (2) As discussed below, the isotropic model m_0 systematically misfits the data, which we call the Rayleigh-Love discrepancy. Thus, we re-invert the Rayleigh and Love wave data for a radially anisotropic model ($V_{SH} \neq V_{SV}$) by searching the restricted parameter space in the vicinity of the initial model, m_0. We compute the final model, m_1, from the Voigt average velocities of the set of accepted V_{SH} and V_{SV} models.

2.2.1. Model parameterization and a priori constraints

One of the principal goals of this study is to determine whether a single, simple parameterization can be found to fit the Rayleigh and Love wave data across the entire US. For this reason, the model parameterization is uniform across the study region. From earlier experience [e.g., *Bensen et al.*, 2009; *Yang et al.*, 2008a], we know that some model complexity is needed to fit broadband dispersion data. There needs to be a well defined sedimentary layer, several crystalline layers in the crust, significant topography on the Moho, smooth vertical variation in the mantle, and the imposition of *a priori* information on sedimentary and crustal thicknesses at least. For this reason, the crustal model comprises a sediment layer underlain by three crystalline crustal layers. The layer thickness ratio for the three crystalline crustal layers is 1:2:2, where the shallowest layer is thinnest. Mantle V_S structure is modeled from the Moho to 250 km depth with five cubic B-splines. Below 250 km, the models tie into the V_S model of *Shapiro and Ritzwoller* [2002]. Where required, water layer depths are constrained by data from the NOAA GEODAS database [NGDC]. In Step 1 of the inversion, we invert for m_0 comprising thirteen independent variables: sediment thickness, crustal thickness, V_S in each crustal layer, V_P/V_S in the sedimentary layer and in the crystalline crust, and five cubic B-spline coefficients (for mantle V_S structure). This inversion is discussed further in section 2.2.2. In Step 2, the inverted variables also include V_{SH} and V_{SV} separately in the middle and lower crustal layers and in the uppermost mantle. Radial anisotropy is allowed only in the middle and lower crust and upper mantle. This inversion produces model m_1, which is discussed in detail in section 2.2.3.

A radially anisotropic medium is represented by five parameters, such as the Love parameters A, C, F, L, and N [*Love*, 1927]. Because surface waves are primarily sensitive to V_{SH} and V_{SV}, which are related to the N and L parameters, respectively, in Step 2 we directly invert for only these parameters and set the remaining parameters at fixed values or determine their values from scaling relationships. We fix the non-dimensional parameters $\phi = C/A = (V_{PH}/V_{PV})^2$, and $\eta = F/(A-2L)$ at unit amplitude, which are their values for an isotropic medium.

In both of the inverted models, density structure is calculated below each grid point using an empirical relation between wave speed and density [*Brocher*, 2005]. The Q model is taken from PREM. Sensitivity tests indicate that reasonable variations in these assumptions have little effect on the strength of the resulting radial anisotropy in the model either because the expected perturbations are small or because perturbations cause both the Rayleigh and Love wave speeds to increase or decrease together and cannot, therefore, resolve the crustal Rayleigh-Love misfit discrepancy, discussed in detail by*Moschetti et al.* [2009].

A 13 – 15 parameter model such as that we construct beneath each grid point is somewhat complicated. It should be understood, however, that because the inversion procedure is a model-space sampling method, the introduction of each extra parameter is met with greater variability (and hence uncertainty) in the other variables determined in the inversion. In order to guarantee physically-reasonable models, it is important to impose *a priori* constraints on the parameter space searched in the inversion. We impose constraints on P- and S-wave speeds as well as sediment and crustal thicknesses. The range of values for V_S and V_P/V_S in the crust and upper mantle is based on previous studies [*Christensen and Mooney*, 1995; *Shapiro and Ritzwoller*, 2002; *Brocher*, 2005]. Because surface waves have little sensitivity to vertical velocity discontinuities, such as exist at the

Moho, sediment and crustal thickness constraints are important to stabilize the velocity structure. Sediment thicknesses are taken from the Global Sediment Model of *Laske and Masters* [1997] but we allow perturbations of up to 250 m. Crustal thickness constraints derive from the receiver function estimates and attendant uncertainties of *Gilbert and Fouch* [2007], where the mean uncertainty in crustal thickness is about 5 km. Model parameterization and constraints are summarized in Fig. 5 and Tables 1 and 2.

An additional important constraint is the requirement that crustal velocities increase monotonically with depth, so that we seek models without a crustal low velocity zone. Crustal low velocity zones actually are expected in some regions, and we point to evidence later that some regions of poor data fit may be improved by relaxing this constraint.

2.2.2. Inversion for the initial isotropic 3D model, $\boldsymbol{m_0}$

Inversion of the local dispersion curves for the initial isotropic model, m_0, is carried out using the Neighbourhood algorithm [*Sambridge*, 1999], and surface wave dispersion curves are calculated using the *Computer Programs in Seismology* package [*Herrmann and Ammon*, 2004]. For an isotropic model, these dispersion curves are verified to be consistent with those from the code MINEOS [*Masters et al.*, 2007]. Each trial model is used to calculate the corresponding Rayleigh wave phase and group and Love wave phase speeds.

The fit of the model-predicted dispersion curves to the local dispersion curves is assessed with the reduced chi-squared misfit parameter, which we refer to as "chi-squared", χ^2:

$$\chi^2 = \frac{1}{n}\sum_{i=1}^{n}\frac{(d_i - p_i)^2}{\sigma_i^2} \tag{3}$$

where n is the total number of discrete periods along the three dispersion curves, d_i and p_i are the observed and model-predicted dispersion values, and σ_i are the data uncertainty values associated with each measurement, as described in Section 2.1.3. We set the threshold for accepting models at two units greater than the value of the best-fitting model, ${\chi^2}_{min}$:

$$ {\chi^2}_{thresh} = {\chi^2}_{min} + 2 \tag{4} $$

Only trial models with corresponding χ^2 values below the threshold value are accepted. The initial isotropic model, m_0, is the mean of the set of accepted models and its uncertainty is the standard deviation of the accepted models at each depth.

2.2.3. Inversion for the radially anisotropic model, $\boldsymbol{m_1}$

To construct the second model, we restrict the parameter space at each grid point to the parameter space defined by the set of accepted models from the isotropic model, m_0. Where the peak-to-peak perturbation of any parameter is less than 10%, the parameter range is set to a ±5% perturbation to the isotropic model, m_0. On average, the restricted parameter space encompasses 65% of the parameter space allowed in the inversion for the initial model, m_0, and is sufficiently large to encompass the structural perturbations needed to fit the data and characterize the trade-offs between different model parameters.

We follow the approach discussed by *Moschetti et al.* [2009] to invert for crustal and mantle radial anisotropy. Crustal anisotropy is introduced to the middle and lower crystalline crustal layers with equal amplitudes $(2\,|V_{SH} - V_{SV}|\,/(V_{SH} + V_{SV}))$. Because the period band of the Rayleigh wave phase speed measurements extends to 100 sec period, these measurements constrain V_{SV} to depths greater than 250 km. However, the Love wave phase speed data used in this inversion have little sensitivity to mantle structures below 60 km depth, and we cannot reasonably constrain V_{SH} below this depth. Although in most other radially anisotropic V_S models the amplitude of radial anisotropy in the upper mantle decreases with depth [*Dziewonski and Anderson*, 1981; *Shapiro and Ritzwoller*, 2002; *Nettles and Dziewonski*, 2008], in our inversion mantle radial anisotropy is represented with a single amplitude from the Moho to 250 km depth. If a PREM-type [*Dziewonski and Anderson*, 1981] mantle anisotropy profile (where the amplitude of radial anisotropy is maximum immediately below the Moho and decreases to zero at 220 km) were to exist in the Earth, our parameterization would overestimate V_{SH}, except in the uppermost mantle. For the amplitudes of mantle anisotropy observed in this model, errors in V_{SH} caused by our parameterization would be less than a 0.5% V_S perturbation above 60 km depth.

Trial models are selected in the inversion by uniform Monte Carlo sampling of the restricted parameter space. The program MINEOS [*Masters et al.*, 2007] is used to calculate the surface wave dispersion curves because it accurately accounts for radial anisotropy in the Earth. However, the calculation of dispersion curves by MINEOS is significantly slower than the calculations for the initial isotropic model, m_0 [*Herrmann and Ammon*, 2004]. To accelerate the inversion, we follow *Shapiro and Ritzwoller* [2002] and employ the method of *James and Ritzwoller* [2004]. 500,000 trial models are sampled from the restricted parameter space at each point. As in the inversion for the initial model, we set the χ^2 threshold for model acceptance at two units greater than the χ^2 value of the best-fitting model. Where the accepted set comprises fewer than 1,000 models, we continue forward modeling until 1,000 models are accepted. Accepted models define the set of models for m_1. The model space of the set of final models, on average, encompasses about 57% of the full parameter space allowed in the inversion for the initial model, m_0. Where the parameter space in the set of final models is not significantly different from the space allowed for the initial inversion (i.e., the model space described by Table 1), we find that those parameters are either poorly sensitive to model perturbations and have high corresponding model uncertainties, or strong parameter trade-offs exist within the model.

2.2.4. Effect of model constraints on the final set of accepted models

The most important effect of the application of model constraints is the imposition of an *a priori* understanding of the Earth. By reducing the allowed model space in the inversion, constraints determine which models are physically plausible. To ensure that the model space search is not too restricted, which would result in the inversion disallowing physically plausible models, we define the model constraints based on observed and estimated parameter ranges of P- and S-wave speeds, crustal and sediment thicknesses, and strength of radial anisotropy [*Christensen and Mooney*, 1995; *Laske and Masters*, 1997; *Shapiro and Ritzwoller*, 2002; *Brocher*, 2005; *Gilbert and Fouch*, 2007; *Nettles and Dziewonski*, 2008]. Model constraints have the greatest effect on the final model where the inversion is not stabilized or where trade-offs in the model parameters exist and the application of model constraints guides selection of trial models. Two examples of the effects of model constraints on the parameter trade-offs in the inversion are presented here. (1) Crustal thickness and lower crustal V_S trade off. An example is in central Nevada (grid point (244.0,39.0)), presented in Fig. 6. At this grid point, crustal thickness and lower crustal V_S in the set of accepted models range over about 10 km and 0.5 km/s, respectively. The insensitivity of the dispersion data to crustal thickness is evidenced by the relatively uniform distribution of values.

(2) Crustal V_P and the strength of radial anisotropy trade off. We find, however, that in the absence of radial anisotropy in the crust, implausible crustal V_P values are required to reduce data misfit. This trade-off is well-known and has previously been documented for mantle radial anisotropy [e.g., *Shapiro and Ritzwoller*, 2002]. Fig. 7 presents the results from two inversions for a grid point in central Nevada (244.0,39.0): one where the model is parametrized as model m_1, described in Table 2 (Fig. 7a), and one where radial anisotropy is not allowed in the crust but V_P/V_S values are allowed to range between 1.5 and 2.0 (Fig. 7b). Although the inversion results of Fig. 7b show that radial anisotropy is not formally required in the crust, V_P values in the crust range from 5.0 — 5.4 km/s and corresponding V_P/V_S values range from 1.54 in the upper crust to 1.59 in the lower crust. Previous studies indicate that these values of V_P and V_P/V_S are too low to be physically plausible [e.g., *Benz et al.*, 1990; *Gilbert and Sheehan*, 2004]. Our preferred inversion result is one where V_P/V_S is constrained by the values of Tables 1 and 2 and radial anisotropy is allowed in the middle and lower crust and in the uppermost mantle. The imposition of physically-defined constraints on V_P/V_S reduces the trade-offs among these parameters and guides the selection of trial models that are used to construct the final model, m_1.

3. 3-D Inversion Results

3.1. Construction of the V_S profiles

Inversion of the local dispersion curves produces a set of 1-D V_{SH} and V_{SV} profiles at each grid point on a 0.5°-by-0.5° grid across the western US. An example of the data fit and of the accepted models from central Nevada (244.0,39.0) is presented in Fig. 8.

An isotropic V_S model is calculated from V_{SH} and V_{SV} by a Voigt average for the case of small anisotropy [*Babuska and Cara*, 1991; *Panning and Romanowicz*, 2006]:

$$V_S = \left(\frac{V_{SH}^2 + 2V_{SV}^2}{3} \right)^{\frac{1}{2}} \tag{5}$$

Isotropic V_S models at each grid point are defined by the set of models calculated from all accepted V_{SH} and V_{SV} profiles. We represent isotropic V_S at each grid point by the mean model, and model uncertainties are presented as the standard deviations of the set of accepted isotropic models about this mean. Isotropic V_S profiles from three tectonic provinces are given in Fig. 9 to provide examples of the variations in velocity structure and uncertainty observed throughout the region.

3.2. V_S model, uncertainties, and the identification of persistent model features

The final 3-D isotropic V_S model comprises the mean V_S model and associated model uncertainties at all grid points. Slices through the V_S model at various depths are plotted in Fig. 10, and the corresponding V_S uncertainties at these depths are presented in Fig. 11. Fig. 12 presents six vertical cross-sections through prominent crustal velocity anomalies in the western US.

Because a reference model is needed to identify velocity anomalies and no appropriate reference model exists for the region, we construct a regional V_S reference model for the western US. Previous studies have made use of global 1-D reference models, such as ak135 [*Kennett et al.*, 1995], but the lower crustal and uppermost mantle velocities observed in the western US are, on average, uniformly slow relative to these models. A western US reference V_S model is constructed from the mean of the V_S models from all continental grid points in the study. It is plotted in Fig. 13 and summarized in Table 3.

The variation of the model laterally is compared to the spatially averaged uncertainty in V_S as a function of depth in Fig. 14. Uncertainties are highest in the shallowest parts of the model, decrease through the upper and middle crust, and increase to values above 3% near the Moho between about 35 and 45 km depth. At these depths, lower crustal V_S trades-off with crustal thickness (as described in Section 2.2.4) and with V_S values in the uppermost mantle, contributing to increased model uncertainties. In the mantle, V_S uncertainties decrease to values between 1% and 1.5% between 60 and 175 km. On average, the root mean square (rms) of model anomalies is more than twice average model uncertainty except in the uppermost mantle between about 30 and 55 km and below 110 km depth. The decreased ratio of rms anomalies to mean uncertainties generally degrades our confidence in model anomalies from the Moho to about 50 km depth and at depths greater than 125 km. *Moschetti et al.* [2009] show that the mean amplitudes ($2\left|V_{SH} - V_{SV}\right| / (V_{SH} + V_{SV})$) of crustal and mantle radial anisotropy beneath the Basin and Range and Northern Rocky Mountains are about 3.5 and 5.5%, respectively. Because mean rms velocity anomalies in the western US are less than about 6%, except near the surface, neglecting the effects of crustal and upper mantle radial anisotropy will bias the estimates of isotropic V_S significantly.

To identify robust features in the V_S model, we interrogate the set of accepted models at each point for persistent model features. In previous discussions of anomaly persistence by *Shapiro and Ritzwoller* [2002] and *Yang et al.* [2008b], persistent model features are defined as those anomalies that exist in all accepted models. We modify this approach by identifying persistent anomalies relative to a reference model by a statistical hypothesis test. We pose as the null hypothesis that the absolute velocity difference between the V_S

model for a given grid point and the western US V_S reference model is less than the V_S uncertainty. Because the means, variances and populations of the western US reference V_S model and the V_S models at all grid points are known, hypothesis testing is readily carried out with a Z-test. Details of the test may be found elsewhere [e.g., *Freund*, 1999]. At grid points where the null hypothesis is rejected at the ! 95% confidence level, model anomalies are termed "persistent". Persistent features in the V_S model are contoured in Fig. 12 with black lines.

We identify here the primary, persistent features in the V_S depth slices. This identification is followed by a brief discussion of the prominent model features in Section 4 below. In the upper crust (Fig. 10a), high wave speeds are observed in the Sierra Nevada, Peninsular Range, Colorado Plateau, northern Cascade Range, and Columbia Plateau. Persistent low wave speeds are observed beneath the Olympic Peninsula, California Coast Range, western Nevada, Wasatch Range, through much of the southern Cascadia backarc region, and beneath the Yakima Fold Belt.

Middle crustal anomalies are presented in Fig. 10b. High wave speeds exist in the Sierra Nevada, Peninsular, and northern Cascade Ranges, throughout the Colorado Plateau, and through much of the Columbia Plateau. At middle crustal depths, high wave speeds emerge throughout the Snake River Plain. Much of central and western Nevada show low wave speeds at middle crustal depths. The low wave speeds beneath the California Coast Ranges, western Nevada, and the Wasatch Range cover a greater area at this depth.

In the lower crust, plotted in Fig. 10c, the most prominent wave speed changes from the overlying crust are the emergence of high velocity features underlying the Peninsular Range, the Great Valley of California, and the region immediately east of the Cascade

Range. The Snake River Plain high velocity anomaly becomes more pronounced, and the broad, middle crustal low velocity anomaly covering much of Nevada and the Cascadia backarc region contracts to distinct bands of low wave speed which run along the northern, eastern, and western boundaries of the Basin and Range. Low wave speeds underlie much of the Northern Rocky Mountain region.

The uppermost mantle V_S structure (plotted at 60 and 100 km depths in Figs. 10d and e) is characterized by four primary features. High velocity anomalies include the subducting Juan de Fuca and Gorda slabs, the Proterozoic lithosphere underlying much of eastern Washington, northern Idaho and western Montana, and a high velocity mantle anomaly associated with the southern Sierra Nevadas and the Transverse Range. Low uppermost mantle wave speeds underlie the region encompassing the Cascadia backarc, the Sierra Nevada, much of Nevada, the Wasatch Range and the Snake River Plain. Uppermost mantle shear-velocities beneath the Snake River Plain and the Cascadia backarc are particularly slow.

3.3. Data misfit from the V_S models

The χ^2 misfit of isotropic model m_0 fis plotted in Fig. 15a. Mean χ^2 misfit is 8.7 across the map. The Basin and Range and the Northern Rocky Mountains show particularly poor data fits. Misfit from this model is analyzed in depth by *Moschetti et al.* [2009], which shows that misfit across the western US results from a crustal Rayleigh-Love wave misfit discrepancy. At these points, the dispersion curves predicted from the isotropic V_S mode, at periods that are most sensitive to the crust are too fast for the Rayleigh wave observations and too slow for the Love wave observations.

Moschetti et al. [2009] also demonstrates that the simultaneous inversion of short period (<30 sec) Rayleigh and Love wave dispersion data from much of the western US requires the introduction of radial anisotropy in the crust and upper mantle to reduce the χ^2 misfit observed from the isotropic V_S model and to resolve the Rayleigh-Love misfit discrepancy. For model m_1, which results from the radially anisotropic V_S inversion, mean χ^2 misfit across the region is reduced to 2.4. The χ^2 values of the best-fitting radially anisotropic V_S models are plotted in Fig. 15b. The dispersion data across 90% of the study region is fit at a χ^2 value of 4 or better by the radially anisotropic V_S model.

Several regions, however, remain poorly fit by a radially anisotropic V_S model with the given model parameterization and a priori constraints. These regions include the Olympic Peninsula, Mendocino Triple Junction, southern Cascadia Backarc, Yakima Fold Belt, Salton Trough, Snake River Plain, California Great Valley, Wasatch Range, and Yellowstone. Because the longer period (> 30 sec) Rayleigh wave measurements are generally well-fit by the radially anisotropic V_S model, we present a plot of χ^2 misfit in the 6 – 30 sec period band in Fig. 15c to highlight the regions where the dispersion measurements with the strongest sensitivities to crustal V_S structure are poorly fit. We refer to the 6 – 30 sec period band χ^2 misfit map, Fig. 15c, as a plot of "crustal misfit".

Characteristic dispersion curve misfits from the radially anisotropic V_S modelm_1 to the dispersion data for the poorly-fit regions are presented in Fig. 16. Because Yellowstone is located at the edge of the inversion region, where the resolution of the dispersion maps degrades, we postpone discussion of this feature until data coverage and resolution in this region improves. Rayleigh wave phase speeds are generally well-fit even in these regions. However, the observed Rayleigh wave phase speeds are slower than model-predicted phase speeds in the Yakima Fold Belt (Fig. 16d) and Great Valley (Fig. 16e). The Rayleigh wave group speeds below about 15 sec period are generally slow relative to the model-predicted values except in the Mendocino Triple Junction (Fig. 16a), Olympic Peninsula (Fig. 16b), and southern Cascadia Backarc (Fig. 16c) regions where the Rayleigh wave group speeds contain local maxima below 20 sec period that are not well-fit by the final V_S model. The Love wave phase speeds below 15 sec period are notably fast, relative to the data for the Olympic Peninsula (Fig. 16b), southern Cascadia Backarc (Fig. 16c) and Snake River Plain (Fig. 16g). Model-predicted Love wave phase speeds are slow at these periods in the Great Valley (Fig. 16e) and Wasatch Range (Fig. 16h). Although the V_S model allows for radial anisotropy in the middle and lower crust, we note that a Rayleigh-Love misfit discrepancy remains in the data misfits from the Yakima Fold Belt and the Wasatch Range (Figs. 16d and h).

We identify two general classes of data misfit in the characteristic data misfit plots in Fig. 16. (1) The first class of structure is at grid points where data misfit is greatest at short periods ($<$ 15 sec) and increases with decreasing period. Because misfit occurs primarily at the shortest periods, where the dispersion curves are most sensitive to the shallowest velocity structures, the model parameterization in the upper and middle crust needs to be modified. Data misfits from the Yakima Fold Belt, Great Valley, Snake River Plain, and Wasatch Range belong to this class. (2) The second class of structure is at grid points where data misfits are greatest at intermediate periods (15 – 30 sec), including the data misfits from the Mendocino Triple Junction, Olympic Peninsula, southern Cascadia Backarc, and Salton Trough regions. In all cases, the models under-predict the Rayleigh wave group speeds between about 10 and 15 sec period. For the first three regions listed, this misfit characteristic in the Rayleigh wave group speeds coincides with a minima in the group speed curves at longer periods ($>$ 25 sec). This intermediate period Airy phase may indicate a small to negative gradient in the V_S depth profile and suggests that crustal low velocity zone parameterizations may be needed. In the Salton Trough region, the shortest ($<$ 10 sec) and longer ($>$ 25 sec) periods are well fit, but the intermediate periods are slow for all wave types. Alternative mid-crustal model parameterizations may be more appropriate for this region.

4. Discussion of the isotropic 3-D V_S model

Although the models m_0 and m_1 include mantle V_S structure, we focus discussion on persistent V_S anomalies in the crust because mantle features have already been discussed by *Yang et al.* [2008b]. The interpretation of all persistent model features is beyond the scope of the paper. In particular, the V_S structure of Cascadia is examined, separately, in *Moschetti and Ritzwoller* [2009]. We identify the following principal, persistent crustal features for discussion here: (1) the California Coast Ranges, Great Valley, and Sierra Nevada Range, (2) the lower crustal velocity anomalies beneath the Cascadia Backarc, Snake River Plain and the High Lava Plains, (3) the crustal structure of the Basin and Range province in Nevada, (4) the enigmatic Yakima Fold Belt and (5) the Colorado Plateau.

4.1. California Coast Ranges, Great Valley, and Sierra Nevada Range

Terrane accretion at the edge of the western Cordillera and emplacement of the Sierra Nevada batholith during Mesozoic arc volcanism led to the development of the present-day California Coast Ranges – Great Valley – Sierra Nevada structures [*Saleeby and Busby-*

Spera, 1992]. In our model, the Coast Ranges throughout California are slow through the upper and middle crust, and the Coast Range lower crust is distinguished from the lower crust beneath the Great Valley by its relatively slower wave speeds. This observation is consistent with the interpretation of later-stage mélange accretion [*Dickinson*, 2008]. Beneath the Great Valley, low wave speeds are associated with the thick sediment packages of the San Joaquin Basin in the south and Sacramento Basin in the north (Figs. 10a and 12a). The Great Valley is underlain by a high velocity lower crust which is offset to the west from the Sierra Nevada Range. This feature underlies the entire Great Valley and has been interpreted as oceanic lithosphere, which may be underlain by continental crust [*Godfrey et al.*, 1997]. The Sierra Nevada Range is bounded to the east by the neutral to low wave speeds in the crust beneath the Walker Lane. There is little variation in shear-velocity with depth within the Sierra Nevada. Although the high wave speeds in the lower crust beneath the Great Valley are persistent model features, the crustal structure in this region will be examined further in future work to reduce data misfit.

4.2. The lower crustal wave speeds of the Cascadia backarc, Snake River Plain, and High Lava Plains

The high wave speed anomalies east of the Cascade arc and beneath the Snake River Plain (see Figs. 12b and 12c) are the most prominent lower crustal velocity features in the northern section of the model. The entire region is underlain by a broad low wave speed anomaly in the uppermost mantle encompassing the Cascadia backarc and Yellowstone hot spot track [*Smith and Braile*, 1994]. The slow wave speeds in the uppermost mantle are strongly correlated with locally high heat flow [*Blackwell and Richards*, 2004], and we infer that the uppermost mantle in this region is relatively warm. Within the Snake

River Plain, *Peng and Humphreys* [1998] and *Stachnik et al.* [2006] find evidence for a mid-crustal sill and a low velocity zone in the lower crust beneath the Snake River Plain caused by the northeastward progression of the Yellowstone hotspot between about 12.5 – 10 Ma [*Pierce and Morgan*, 1989]. Our model is consistent with the interpretation of emplacement of high velocity material in the middle to lower crust that is perhaps chemically distinct from surrounding crust. Although data misfit from our model is not improved by allowing a crustal low velocity zone with the current crustal parameterization, the relatively high crustal misfits through the Snake River Plain and southern Cascadia backarc region suggest that modifications in the parameterization of the crustal velocity structure in this region is warranted.

Previous seismic studies have variously interpreted the high wave speed lower crustal anomaly, which runs along the entire eastern edge of the Cascade Range in our model, as Mesozoic subduction zone backstop and magmatic arc [*Fuis*, 1998; *Fuis et al.*, 1987], crustal underplating [*Catchings and Mooney*, 1988] and as a lower crustal intrusion and modification caused by continental rifting [*Catchings and Mooney*, 1988]. We propose that the high velocity lower crustal features east of the Cascade Range and within the Snake River Plain result from mafic crustal intrusions or crustal underplating caused by partial melting of warm uppermost mantle. Across this region, the lower crust beneath eastern Oregon is distinguished by its reduced wave speed relative to neighboring high velocity anomalies.

The High Lava Plains of southeastern Oregon have experienced recent volcanism along a northwest younging track which mirrors the Yellowstone hotspot-related calderas of the Snake River Plain [*Jordan et al.*, 2004]. The relatively depressed wave speeds of the lower crust in this region may result from compositional and/or thermal modifications to the crust caused by magma injection or conductive heating. The region has been extensively studied in recent years [e.g., *Xue and Allen*, 2006; *Roth et al.*, 2008; *Warren et al.*, 2008]. Fig. 12c presents a cross-section through the region, along 44°N latitude from the Cascade Range to the western Snake River Plain, which shows the neutral lower crustal wave speeds beneath eastern Oregon that increase to the west and east.

4.3. Crustal structure of the Basin and Range in northern Nevada

Nevada has experienced a complex geologic history, including significant crustal deformation. The Basin and Range province is currently extending at about 1 cm/yr [*Thatcher et al.*, 1999] and has extended by about a factor of two during the late Cenozoic Era [*Wernicke*, 1992]. However, the isotropic V_S model shows relatively uniform crustal and mantle structure across northern Nevada at 39.5° latitude (see Fig. 12d). Mean middle and lower crustal V_S values are about 3.4 and 3.6 km/s, respectively. Previous studies have identified the presence of a strongly reflecting lower crustal body throughout much of Nevada and a thin, very high wave speed anomaly at the base of the crust [*Potter et al.*, 1987; *McCarthy and Thompson*, 1988; *Benz et al.*, 1990]. We find no evidence in the isotropic V_S values of the model for large velocity discontinuities in the crust. However, as discussed by *Moschetti et al.* [2009], the correlation between the regions with high amplitudes of crustal radial anisotropy and significant Cenozoic extension, which is consistent with the alignment of anisotropic crustal minerals, may be a cause for the reflective lower crust [*McCarthy and Thompson*, 1988]. No evidence for a thin high velocity layer at the base of the crust exists in our model. We acknowledge, however, that the crust may contain finer-scale structures than cannot be resolved with surface waves.

4.4. Yakima Fold Belt

The distinctive crustal velocity structure of the Yakima Fold Belt arises from the effects of volcanic flows and deformation on a deep sedimentary basin [*Campbell and Bentley*, 1981]. Fig. 12e presents a cross-section from the Cascade Range, through the Yakima Fold Belt, to the Columbia Plateau in eastern Washington. Within the Yakima Fold Belt, our model shows very low wave speeds in the middle crust and low wave speeds in the upper crust. This structure has been interpreted to result from the capping of a deep sedimentary basin by basalt flows of the Columbia River Basalt Group between about 17 – 14.5 Ma [*Catchings and Mooney*, 1988; *Tolan et al.*, 1989]. The decreased wave speeds of the lower crust, which overlie the Proterozoic mantle lithosphere beneath eastern Washington, suggest that lower crustal modification in this region was impeded by the resistant mantle lithosphere. *Catchings and Mooney* [1988] imaged the sediments of the Pasco Basin, which underlie 3 – 6 km of basalt, and a high velocity lower crustal body. They proposed that the structure results from continental rifting. Our model is generally consistent with their observations, but our observation that the high velocity lower crustal feature extends along the entire Cascade Range suggests that the high wave speed anomaly in the lower crust beneath the Yakima Fold Belt may be caused by widespread crustal intrusions and underplating related to the dynamics of the Cascadia subduction zone. Because of the large data misfit in this region, the model parameterization for this feature will be considered futher in future work.

4.5. Colorado Plateau

Fig. 12f presents a cross-section along 247.5° longitude, which traverses the western Colorado Plateau from south to north. The crust throughout the Colorado Plateau shows little variation in V_S with depth. At upper and middle crustal depths, V_S is fast and has been inferred to result from a mafic composition in the plateau [*Zandt et al.*, 1995]. North of the plateau, the crustal wave speeds of the Wasatch Range are uniformly low. The low wave speeds of the uppermost mantle that flank the Colorado Plateau are consistent with observations of late Cenozoic basaltic eruptions [*Best and Brimhall*, 1974]. At the southern end of the cross-section, the transition zone between the southern Basin and Range province and the Colorado Plateau shows neutral to low wave speeds in the middle to lower crust. It remains unclear whether the lower crustal wave speeds adjacent to the Colorado Plateau result from thermal or compositional effects.

4.6. Anomalous misfit regions

Although 90% of the study region is fit by a simple V_S model of the crust and uppermost mantle, high data misfits remain at 10% of the model grid points. The grid points with significant misfit at the short periods consistent with a crustal origin can be organized into eight geologic regions: (1) the Olympic Peninsula, (2) Mendocino Triple Junction, (3) southern Cascadia Backarc and High Lava Plains, (4) Yakima Fold Belt, (5) Salton Trough, (6) Snake River Plain, (7) California Great Valley, and (8) Wasatch Range. Because these regions are geologically complex and the current model parameterization is not able to fit the observed data well, further investigation into the V_S structure of these regions is required.

We suggest three modifications to the current model parameterization to improve the data misfit from these regions: (1) breaking the constraint that crustal shear-velocities increase monotonically with depth, (2) introducing thinner crustal layers, and (3) including the effect of radial anisotropy in the upper crust. Except in California's Great Valley, where sediment thicknesses are significantly greater than average, sensitivity tests suggest that perturbations to the V_S structure of the sediment layer are unlikely to resolve the observed data misfits. The first data misfit class, defined in Section 3.3, is likely to show improved fit to the data by modifying the parameterization of the upper to middle crustal layers. In contrast, the second data misfit class is likely to be improved by varying model parameterization at the depths of the middle and lower crustal layers. *Moschetti and Ritzwoller* [2009] examine the effect on χ^2 misfit of breaking the monotonic crustal velocity constraint within the Cascadia Forearc, Arc and Backarc regions and find that the misfit to the dispersion data from the Cascadia Forearc beneath northern California is improved by the introduction of a crustal low velocity zone.

5. Conclusions

A radially anisotropic inversion of Rayleigh and Love wave dispersion measurements from ANT and MPWT is carried out to construct an isotropic 3-D V_S model of the crust and uppermost mantle beneath the western US. Because the data are inverted by a Monte Carlo method, model uncertainties accompany the model and allow for the identification of persistent model features by statistical hypothesis testing. Model uncertainties peak below the Moho and reduce confidence in the uppermost mantle V_S estimates from the base of the crust to about 55 km depth, but persistent isotropic anomalies exist at all crustal depths across the western US.

Although the velocity structure of the upper mantle beneath the western US consists of only four principal large-scale shear-velocity features, the overlying continental crust contains far greater heterogeneity. We infer that the high wave speed anomalies of the lower crust result primarily from mafic compositions caused by intrusion, underplating or accretion. The low wave speed anomalies of the lower crust beneath the Basin and Range, High Lava Plains and eastern California are inferred to be thermally-depressed wave speed features caused by conductive heating. At middle crustal depths, accretionary prisms and mélange show the lowest wave speeds. Middle crustal high wave speed anomalies are caused by both compositional effects, for example, the basalts of the Columbia River flood basalt group and throughout the Snake River Plain, and crystalline effects, as seen in the granitoids of the Sierra Nevada. In general, the upper and middle crustal wave speed anom! alies are correlated. Prominent exceptions to this correlation include the Snake River Plain, Northern Rocky Mountains and eastern Basin and Range. The velocity structure of the middle and lower crust beneath the Snake River Plain is consistent with a mafic intrusion caused by the passing Yellowstone hotspot. The cause of the wave speed differences in the upper and middle- to lower-crust beneath the Northern Rocky Mountains and the Basin and Range remains enigmatic. The amplitudes of the observed velocity anomalies are similar to the amplitudes of radial anisotropy for the crust and uppermost mantle found by *Moschetti et al.* [2009], so that radial anisotropy cannot be ignored in the construction of an isotropic V_S model either in the crust or upper mantle.

The vast majority of the western US is well fit by a radially anisotropic V_S model with the parameterization discussed in Section 2.2.1 and where crustal velocities increase monotonically with depth. However, this simple model parameterization is not sufficient to fit all dispersion curves in the western US, and high crustal misfit is observed in the Olympic Peninsula, Mendocino Triple Junction, southern Cascadia Backarc, Yakima Fold Belt, Salton Trough, Snake River Plain, California Great Valley, and Wasatch Range. Future work is needed to investigate the effect of different crustal parameterizations on data misfit in these regions. The inversion method presented here naturally lends itself to the incorporation of longer period ($>$ 32 sec) Love wave measurements for improved constraints on mantle radial anisotropy and to the inversion of emerging data from the TA to extend the model to a continental-scale crustal V_S model.

Acknowledgments. We thank Malcolm Sambridge for the Neighbourhood algorithm code. Research support from the National Science Foundation (NSF) (EAR-0450082 and EAR-0711526) and an NDSEG Fellowship from the American Society for Engineering Education to M.P.M. are acknowledged. The facilities of the IRIS Data Management System, and specifically the IRIS Data Management Center, were used to access the waveform and metadata required in this study. The IRIS DMS is funded by the NSF and specifically the GEO Directorate through the Instrumentation and Facilities Program of the NSF under Cooperative Agreement EAR-0552316.

References

Babuska, V., and M. Cara (1991), *Seismic Anisotropy in the Earth*, Kluwer Academic Publishers, Dordrecht.

Barmin, M. P., M. H. Ritzwoller, and A. L. Levshin (2001), A fast and reliable method for surface wave tomography, *Pure Appl. Geophys.*, *158*(8), 1351–1375.

Bensen, G. D., M. H. Ritzwoller, M. P. Barmin, A. L. Levshin, F. Lin, M. P. Moschetti, N. M. Shapiro, and Y. Yang (2007), Processing seismic ambient noise data to obtain reliable broad-band surface wave dispersion measurements, *Geophys. J. Int.*, *169*, 1239–1260.

Bensen, G. D., M. H. Ritzwoller, and N. M. Shapiro (2008), Broad-band ambient noise surface wave tomography across the United States, *J. Geophys. Res.*, *113*(B05306).

Bensen, G. D., M. H. Ritzwoller, and Y. Yang (2009), A 3D shear velocity model of the crust and uppermost mantle beneath the United States from ambient seismic noise, *Geophys. J. Int.*, *117*(3).

Benz, H. M., R. B. Smith, and W. D. Mooney (1990), Crustal structure of the northwestern Basin and Range province from the 1986 program for array seismic studies of the continental lithosphere seismic experiment, *J. Geophys. Res.*, *95*(B13), 21,823–21,842.

Best, M. G., and W. H. Brimhall (1974), Late Cenozoic alkalic basaltic magmas in the western Colorado Plateaus and the Basin and Range Transition Zone, U.S.A., and their bearing on mantle dynamics, *GSA Bulletin*, *85*(11), 1677–1690.

Blackwell, D. D., and M. Richards (2004), Geothermal map of North America, *American Assoc. Petroleum Geologist (AAPG), 1 sheet, scale 1:6,500,000.*

Brenguier, F., N. M. Shapiro, M. Campillo, A. Nercessian, and V. Ferrazzini (2007), 3-D surface wave tomography of the Piton de la Fournaise volcano using seismic noise correlations, *Geophys. Res. Lett.*, *34*(L02305).

Brocher, T. (2005), Empirical relations between elastic wavespeeds and density in the Earth's crust, *Bull. Seism. Soc. Am.*, *95*(6), 2081–2092.

Burdick, S., C. Li, V. Martynov, T. Cox, J. Eakins, L. Astiz, F. Vernon, G. Pavlis, and R. van der Hilst (2008), Upper mantle heterogeneity beneath North America from travel time tomography with global and USArray Transportable Array data, *Seism. Res. Lett.*, *79*(3), 384–392.

Campbell, N. P., and R. D. Bentley (1981), Late Quaternary deformation of the Toppenish Ridge uplift in south-central Washington, *Geology*, *9*, 519–524.

Catchings, R. D., and W. D. Mooney (1988), Crustal structure of east central Oregon: relation between Newberry Volcano and regional crustal structure, *J. Geophys. Res.*, *93*(B9), 10,081–10,094.

Catchings, R. D., and W. D. Mooney (1988), Crustal structure of the Columbia Plateau: Evidence for Continental Rifting, *J. Geophys. Res.*, *93*(B1), 459–474.

Cho, K. H., R. B. Herrmann, C. J. Ammon, and K. Lee (2007), Imaging the Upper Crust of the Korean Peninsula by Surface-Wave Tomography, *Bull. Seism. Soc. Am.*, *97*(18), 198–207.

Christensen, N., and W. D. Mooney (1995), Seismic velocity structure and composition of the continental crust: A global view, *J. Geophys. Res.*, *100*(B6), 9761–9788.

Dickinson, W. R. (2008), Accretionary Mesozoic-Cenozoic expansion of the Cordilleran continental margin in California and adjacent Oregon, *Geosphere*, *4*(2), 329–353.

Dziewonski, A. M., and D. L. Anderson (1981), Preliminary reference Earth model, *Phys. Earth Plan. Int.*, *25*(4), 297–356.

Forsyth, D. W., and A. Li (2005), Array-analysis of two-dimensional variations in surface wave phase velocity and azimuthal anisotropy in the presence of multipathing interference, in *Seismic Earth: Array Analysis of Broadband Seismograms*, vol. 157, edited by A. Levander and G. Nolet, pp. 81–97, AGU.

Freund, J. (1999), *Mathematical Statistics: 6th Edition*, Prentice Hall, Upper Saddle River, NJ.

Fuis, G. (1998), West margin of North America – a synthesis of recent seismic transects, *Tectonophysics*, *288*(1–4), 265–269.

Fuis, G., T. Ryberg, N. Godfrey, D. Okaya, and J. Murphy (2001), Crustal structure and tectonics from the Los Angeles basin to the Mojave Desert, southern California, *Geology*, *29*(1), 15–18.

Fuis, G. S., J. J. Zucca, W. D. Mooney, and B. Milkereit (1987), A geologic interpretation of seismic-refraction results in northeastern California, *GSA Bulletin*, *98*(1), 53–65.

Gilbert, H. J., and M. Fouch (2007), Complex upper mantle seismic structure across the southern Colorado Plateau/Basin and Range II: Results from receiver function analysis, *Eos Trans. AGU*, *88*(S41B-0558).

Gilbert, H. J., and A. F. Sheehan (2004), Images of crustal variations in the intermountain west, *J. Geophys. Res.*, *109*(B03306).

Godfrey, N. J., B. C. Beaudoin, S. L. Klemperer, and M. W. Group (1997), Ophiolitic basement to the Great Valley forearc basin, California, from seismic and gravity data: Implications for crustal growth at the North American continental margin, *GSA Bul-*

letin, *108*(12), 1536–1562.

Grand, S. P. (1994), Mantle shear structure beneath the Americas and surrounding oceans, *J. Geophys. Res.*, *99*(B6), 11,591–11,621.

Herrmann, R. B., and C. J. Ammon (2004), *Computer programs in seismology: Surface waves, receiver functions and crustal structure*, St. Louis University, St. Louis, MO.

James, M. B., and M. H. Ritzwoller (1999), Feasibility of truncated perturbation expansions to approximate Rayleigh wave eigenfrequencies and eigenfunctions in heterogeneous media, *Bull. Seism. Soc. Am.*, *89*, 433–442.

Jordan, B., A. Grunder, R. Duncan, and A. Deino (2004), Geochronology of age-progressive volcanism of the Oregon High Lava Plains: Implications for the plume interpretation of Yellowstone, *J. Geophys. Res.*, *109*(B10202).

Kennett, B. L. N., E. R. Engdahl, and R. Buland (1995), Constraints on seismic velocities in the Earth from traveltimes, *Geophys. J. Int.*, *122*(1), 108–124.

Laske, G., and G. Masters (1997), A global digital map of sediment thickness, *EOS Trans. AGU*, *78*, 483.

Lin, F., M.H. Ritzwoller, J. Townend, M. Savage, S. Bannister (2007), Ambient noise Rayleigh wave tomography of New Zealand, *Geophys. J. Int., 170*(2), 649-666.

Lin, F., M. P. Moschetti, and M. H. Ritzwoller (2008), Surface wave tomography of the western United States from ambient seismic noise: Rayleigh and Love wave phase velocity maps, *Geophys. J. Int.*, *173*(1), 281–298.

Lin, F., M. H. Ritzwoller, and R. Snieder (2009), Eikonal tomography: Surface wave tomography by phase-front tracking across a regional broad-band seismic array, *Geophys. J. Int.*, *177*(3), 1091–1110.

Lobkis, O. I., and R. L. Weaver (2001), On the emergence of the Green's function in the correlations of a diffuse field, *J. Acous. Soc. Am.*, *110*(6), 3011–3017.

Love, A. (1927), *A Treatise on the Theory of Elasticity, 4th Ed.*, Cambridge Univ., Cambridge.

Marone, F., Y. Gung, and B. Romanowicz (2007), Three-dimensional radial anisotropic structure of the North American upper mantle from inversion of surface waveform data, *Geophys. J. Int.*, *171*(1), 206–222.

Masters, G., M. P. Barmine, and S. Kientz (2007), Mineos user's manual, *Computational Infrastructure for Geodynamics*.

McCarthy, J., and G. A. Thompson (1988), Seismic imaging of extended crust with emphasis on the Western United States, *Geol. Soc. Am. Bull.*, *100*(9), 1361–1374.

Moschetti, M. P., and M. H. Ritzwoller (2009), Lower crustal fluids in the Cascadia forearc: insight from surface wave tomography, *Geophys. Res. Lett.*, in preparation.

Moschetti, M. P., M. H. Ritzwoller, and N. M. Shapiro (2007), Surface wave tomography of the western United States from ambient seismic noise: Rayleigh wave group velocity maps, *Geochem. Geophys. Geosys.*, *8*(Q08010).

Moschetti, M. P., M. H. Ritzwoller, F.-C. Lin, and Y. Yang (2009), Seismic evidence for widespread deep crustal deformation caused by extension in the western US, *Nature*, submitted.

Nettles, M., and A. M. Dziewonski (2008), Radially anisotropic shear velocity structure of the upper mantle globally and beneath north america, *J. Geophys. Res.*, *113*(B02303).

NGDC (2009), *Marine Trackline Geophysics*, National Geophysical Data Center, NESDIS, NOAA, http://map.ngdc.noaa.gov/website/mgg/trackline/viewer.htm.

Panning, M., and B. Romanowicz (2006), A three dimensional radially anisotropic model of shear velocity in the whole mantle, *Geophys. J. Int.*, *167*.

Peng, X., and E. D. Humphreys (1998), Crustal velocity structure across the eastern Snake River Plain and Yellowstone swell, *J. Geophys. Res.*, *103*(B1), 7171–7186.

Pierce, K. L., and W. J. Morgan (1989), The track of the Yellowstone hotspot: volcanism, faulting, and uplift, in *Regional Geology of Eastern Idaho and Western Wyoming*, edited by P. Link, M. Kuntz, and L. Platt, pp. 1–53, Geol. Soc. Amer. Memoir 179.

Pollitz, F. F. (2008), Observations and interpretation of fundamental mode Rayleigh wavefields recorded by the Transportable Array (USArray), *Geophys. J. Int.*, *173*, 189–204.

Potter, C. J., et al. (1987), Crustal structure of north-central Nevada; results from COCORP deep seismic profiling, *Geol. Soc. Am. Bull.*, *98*(3), 330–337.

Ramachandran, K., R. D. Hyndman, and T. M. Brocher (2006), Regional p wave velocity structure of the northern Cascadia subduction zone, *J. Geophys. Res.*, *111*(B12301).

Roth, J. B., M. J. Fouch, D. E. James, and R. W. Carlson (2008), Three-dimensional seismic velocity structure of the northwestern United States, *Geophys. Res. Lett.*, *35*(L15304).

Sabra, K. G., P. Gerstoft, P. Roux, W. A. Kuperman, and M. C. Fehler (2005), Extracting time-domain Green's function estimates from ambient seismic noise, *Geophys. Res. Lett.*, *32*, 3310–3313.

Saleeby, J. B., and C. Busby-Spera (1992), Early Mesozoic tectonic evolution of the western U.S. Cordillera, in *The Cordilleran Orogen: Conterminous US*, edited by B. C. Burchfiel, P. Lipman, and M. Zoback, Geol. Soc. Amer., Boulder, CO.

Sambridge, M. (1999), Geophysical inversion with a neighbourhood algorithm – I. Searching a parameter space, *Geophys. J. Int.*, *138*(2), 479–494.

Shapiro, N. M., and M. Campillo (2004), Emergence of broadband Rayleigh waves from correlations of the ambient seismic noise, *Geophys. Res. Lett.*, *31*(7), 7614–7617.

Shapiro, N. M., and M. H. Ritzwoller (2002), Monte-Carlo inversion for a global shear-velocity model of the crust and upper mantle, *Geophys. J. Int.*, *151*(1), 88–105.

Shapiro, N. M. M. Campillo, L. Stehly, and M. H. Ritzwoller (2005), High resolution surface wave tomography from ambient seismic noise, *Science, 307*(5715), 1615-1618.

Smith, R. B., and L. W. Braile (1994), The Yellowstone hotspot, *Journal of volcanology and geothermal research*, *61*(3–4), 121–187.

Snieder, R. K. (2004), Extracting the Green's function from the correlation of coda waves: A derivation based on stationary phase, *Phys. Rev. E*, *69*(4), 046,610(8).

Stachnik, J. C., K. Dueker, D. L. Schutt, and H. Yuan (2006), Imaging Yellowstone plume-lithosphere interactions from inversion of ballistic and diffusive Rayleigh wave dispersion and crustal thickness data, *Geochem. Geophys. Geosys.*, *9*(6), Q06,004.

Stehly, L., B. Fry, M. Campillo, N. M. Shapiro, J. Guilbert, L. Boschi, and D. Giardini (2009), Tomography of the Alpine region from observations of seismic ambient noise, *Geophys. J. Int.*, *178*(1), 338–350.

Tanimoto, T., and K. P. Sheldrake (2002), Three-dimensional S-wave velocity structure in Southern California, *Geophys. Res. Lett.*, *29*(8), 64–68.

Thatcher, W., G. R. Foulger, B. R. Julian, J. Svarc, E. Quilty, and G. W. Bawden (1999), Present-Day Deformation Across the Basin and Range Province, Western United States, *Science*, *283*(5408), 1714–1718.

Tolan, T. L., S. P. Reidel, M. H. Beeson, J. L. Anderson, K. R. Fecht, and D. A. Swanson (1989), Revisions to the estimates of the areal extent and volume of the Columbia River Basalt Group, in *Volcanism and tectonism in the Columbia River Flood Basalt Province*, edited by S. P. Reidel and P. R. Hooper, pp. 1–20, spec. Pap. Geol. Soc. Am., 239.

van der Lee, S., and A. Frederiksen (2005), Surface wave tomography applied to the North American upper mantle, *Geophysical monograph*, *157*, 67–80.

Villasenor, A., Y. Yang, M. H. Ritzwoller, and J. Gallart (2007), Ambient noise surface wave tomography of the Iberian Peninsula: Implications for shallow seismic structure, *Geophys. Res. Lett.*, *34*, L11304.

Wapenaar, K. (2004), Retrieving the elastodynamic Green's function of an arbitrary inhomogeneous medium by cross correlation, *Phys. Rev. Lett.*, *93*(25), 254,301(4).

Warren, L. M., J. A. Snoke, and D. E. James (2008), S-wave velocity structure beneath the High Lava Plains, Oregon, from Rayleigh-wave dispersion inversion, *Earth Planet. Sci. Lett.*, *274*(1–2), 121–131.

Weaver, R. L., and O. I. Lobkis (2001), Ultrasonics without a source: Thermal fluctuation correlations at MHz frequencies, *Phys. Rev. Lett.*, *87*(13), 134,301(4).

Wernicke, B. (1992), Cenozoic extensional tectonics of the u.s. cordillera, in *The Cordilleran Orogen: Conterminous US*, edited by B. C. Burchfiel, P. Lipman, and M. Zoback, Geol. Soc. Amer., Boulder, CO.

West, J. D., M. J. Fouch, J. B. Roth, and L. T. Elkins-Tanton (2009), Vertical mantle flow associated with a lithospheric drip beneath the Great Basin, *Nature Geoscience*, *2*.

Xue, M., and R. Allen (2006), Origin of the Newberry Hotspot Track: Evidence from shear-wave splitting, *Earth Planet. Sci. Lett.*, *244*, 315–322.

Yan, Z., and R. W. Clayton (2007), Regional mapping of the crustal structure in southern California from receiver function, *J. Geophys. Res.*, *112*(B05311).

Yang, Y., M. H. Ritzwoller, A. L. Levshin, and N. M. Shapiro (2007), Ambient noise Rayleigh wave tomography across Europe, *Geophys. J. Int.*, *168*(1), 259–274.

Yang, Y., A. Li, and M. H. Ritzwoller (2008a), Crustal and uppermost mantle structure in southern Africa revealed from ambient noise and teleseismic tomography, *Geophys. J. Int.*, *174*(1), 235–248.

Yang, Y., M. H. Ritzwoller, F.-C. Lin, M. Moschetti, and N. Shapiro (2008b), The structure of the crust and uppermost mantle beneath the western US revealed by ambient noise and earthquake tomography, *J. Geophys. Res.*, *113*(B12310).

Yao, H., R. D. V. der Hilst, and M. V. de Hoop (2006), Surface-wave array tomography in SE Tibet from ambient seismic noise and two-station analysis – I phase velocity maps, *Geophys. J. Int.*, *166*, 732–744.

Yao, H., C. Beghein, and R. D. van der Hilst (2007), Surface-wave array tomography in SE Tibet from ambient seismic noise and two-station analysis: II crustal and upper mantle structure, *Geophys. J. Int.*, *173*, 205–219.

Zandt, G., S. C. Myers, and T. C. Wallace (1995), Crust and mantle structure across the Basin and Range–Colorado Plateau boundary at 37N latitude and implications for Cenozoic extensional mechanism, *J. Geophys. Res.*, *100*(B6), 10,52–10,548.

Zheng, S. H., X. L. Sun, X. D. Song, Y. Yang, and M. H. Ritzwoller (2008), Surface wave tomography of China from ambient seismic noise correlation, *Geochem. Geophys. Geosys.*, *9*(Q05020).

Table 1. Model parameter constraints for the isotropic initial model, m_0

Model parameter	Range	Source
Sediment thickness	± 250 m	LM1997
Crustal thickness	± 5 km	GF2007
Layer thickness ratio, crystalline crust	1:2:2	
V_S, sediments	1.5 – 3.0 km/s	CM1995 and B2005
V_S, upper crust	2.0 – 3.5 km/s	CM1995 and B2005
V_S, middle and lower crust	2.5 – 4.0 km/s	CM1995 and B2005
V_P/V_S, sediment layer	1.75 – 2.5 km/s	B2005
V_P/V_S, crystalline crust (same in all layers)	1.70 – 1.8 km/s	B2005
V_P/V_S, mantle	1.8 km/s	SR2002
V_S, upper mantle	3.7 – 4.75 km/s	SR2002

B2005 – *Brocher* [2005]
CM1995 – *Christensen and Mooney* [1995]
GF2007 – *Gilbert and Fouch* [2007]
LM1997 – *Laske and Masters* [1997]
SR2002 – *Shapiro and Ritzwoller* [2002]

Table 2. Model parameter constraints for the radially-anisotropic model, m_1

Model parameter	Minimum range	Source
Sediment thickness	± 250 m	LM1997
Crustal thickness	± 5 km	GF2007
Layer thickness ratio, crystalline crust	1:2:2	
V_S, sediments	†	
V_S, upper crust	†	
V_S, middle crust	†	
V_S, lower crust	†	
V_P/V_S, sediment layer	†	
V_P/V_S, crystalline crust	†	
V_P/V_S, mantle	†	
V_S, upper mantle	†	
Radial anisotropy, sediment and upper crust	0%	MRLY2009
Radial anisotropy, middle and lower crust	Unconstrained	MRLY2009
Radial anisotropy, upper mantle	≤ 10%	ND2008

†: at least ±5% from model m_0 GF2007 – *Gilbert and Fouch* [2007]
LM1997 – *Laske and Masters* [1997]
MRLY2009 – *Moschetti et al.* [2009]
ND2008 – *Nettles and Dziewonski* [2008]

Table 3. Western US reference V_S crustal model

Model Parameter	Value
Sediment thickness	750 m
Crustal thickness	32.0 km
V_S sediments	1.95 km/s
V_S layer 1	3.27 km/s
V_S layer 2	3.47 km/s
V_S layer 3	3.74 km/s
V_P/V_S sediment layer	2.10 km/s
V_P/V_S crystalline crust	1.78 km/s

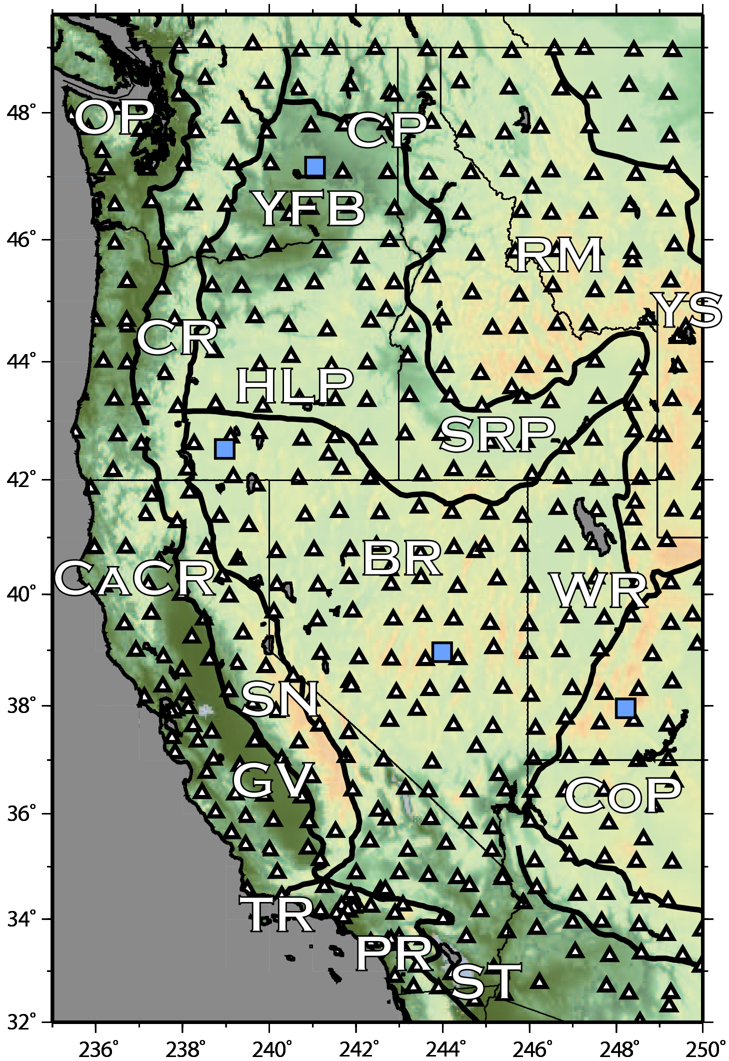

Figure 1. Western US inversion area, showing Transportable Array (TA) and other stations utilized in this study. Major physiographic regions are outlined with bold black lines. Geologic and tectonic features in the region include the Olympic Peninsula (OP), CoP (Columbia Plateau), Yakima Fold Belt (YFB), Rocky Mountains (RM), Basin and Range (BR), California Coast Ranges (CaCR), Great Valley (GV), High Lava Plains (HLP), Sierra Nevada (SN), Transverse Range (TR), Peninsular Range (PR), Cascade Range (CR), Snake River Plain (SRP), Wasatch Range (WR), Yellowstone (YS) and Salton Trough (ST). The grid point locations for coordinates (239.0,42.5), (241.0,47.0), (248.0,38.0) and (244.0, 39.0), discussed in Figs. 5 – 8, are plotted with blue squares.

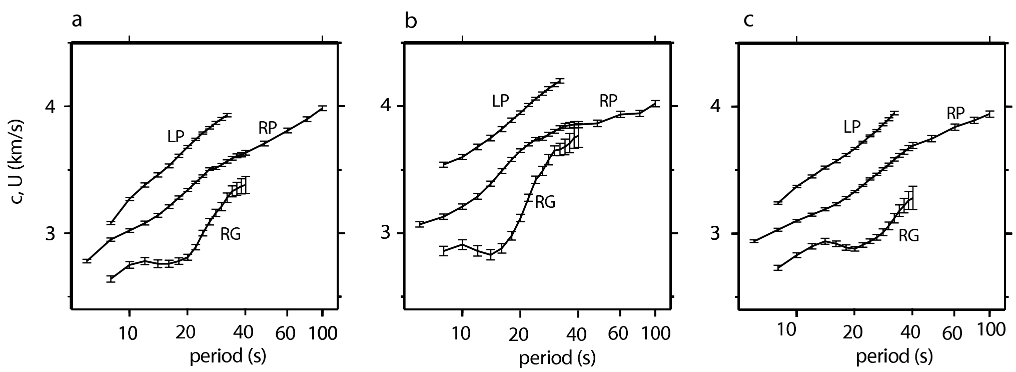

Figure 2. Dispersion curves and associated uncertainty values from (a) the southern Cascadia Backarc (239.0,42.5), (b) the Yakima Fold Belt (241.0,47.0), and (c) the Colorado Plateau (248.0,38.0). Locations of these grid points are identified in Fig. 1. RP, RG and LP refer to the Rayleigh wave phase and group speeds and Love wave phase speeds, respectively.

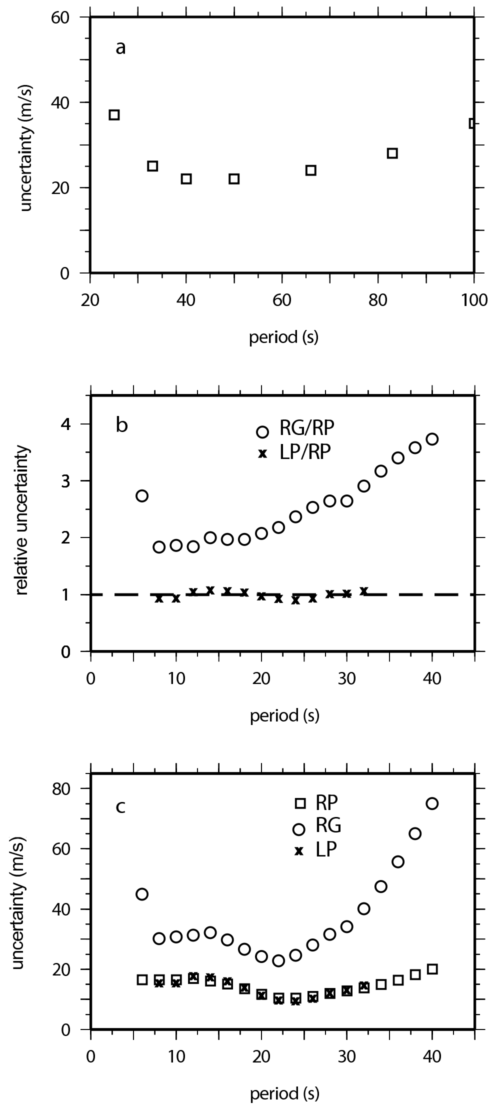

Figure 3. Uncertainties in Rayleigh wave phase and group and Love wave phase speeds. (a) Rayleigh wave phase speed uncertainties from MPWT. Mean uncertainty is 27.6 km/s. (b) Estimates of the ratios of uncertainties determined from the temporal variation in the inter-station dispersion measurements averaged over all measurements. Circles and crosses represent the ratios $\sigma^{RG}(T)/\sigma^{RP}(T)$ and $\sigma^{LP}(T)/\sigma^{RP}(T)$, respectively. RP, RG, and LP refer to Rayleigh wave phase and group and Love wave phase speeds, respectively. (c) Spatially-averaged Rayleigh wave phase and group speed uncertainties are plotted with squares and circles, respectively. The Love wave phase speed uncertainties are plotted with crosses. Mean uncertainty values for the Rayleigh wave phase and group speed and Love wave phase speed are 14.5, 36.8, and 13.4 m/s, respectively.

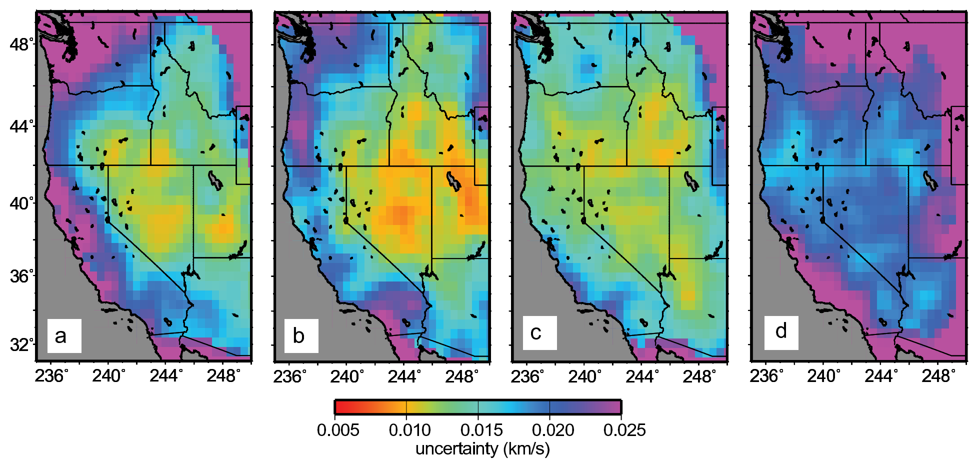

Figure 4. Rayleigh wave phase speed uncertainties for ANT are taken from the Eikonal tomography uncertainty estimates of *Lin et al.* [2009]. Examples are plotted at (a) 8, (b) 16, (c) 30, and (d) 40 sec periods.

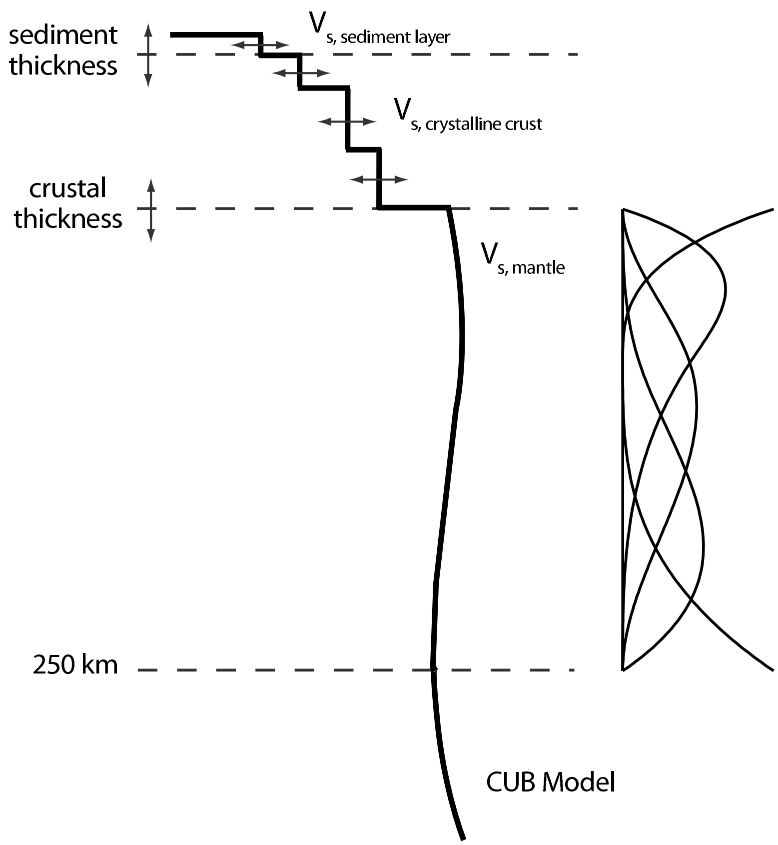

Figure 5. Depiction of the model parameterization. The models m_0 and m_1 are parameterized with four crustal layers and five cubic B-splines in the mantle to 250 km depth. Crustal layers include a sedimentary layer and three crystalline layers. The thickness ratio of the crystalline crustal layers is fixed at 1:2:2. Sediment and crustal thickness perturbations are allowed. Crustal velocities are required to increase monotonically with depth. Below 250 km depth, the model ties into the V_S model of *Shapiro and Ritzwoller* [2002]. Model m_1 includes radial anisotropy ($V_{SH} \neq V_{SV}$) in the middle and lower crust and in the upper mantle (not shown).

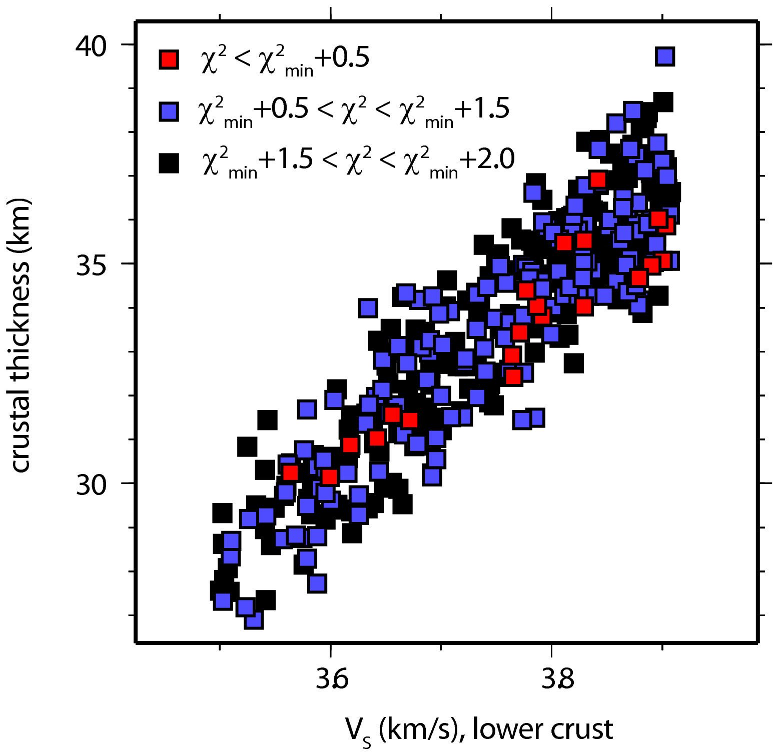

Figure 6. Trade-off between lower crustal V_S and crustal thickness for a point in central Nevada (244.0,39.0) from model m_1. Crustal thicknesses range over more than 10 km and lower crustal V_S ranges over 0.5 km/s in the set of accepted models.

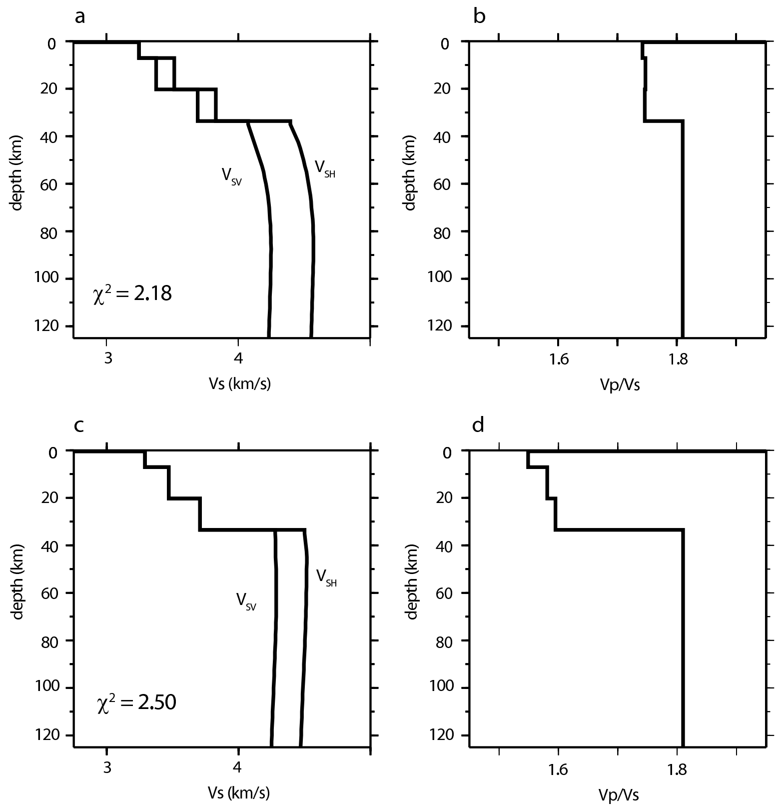

Figure 7. Effect of V_P/V_S on the strength of radial anisotropy in the crust at a location in central Nevada (244.0,39.0). The (a) V_S and (b) V_P/V_S models that result from an inversion where the model includes radial anisotropy in the crust and upper mantle and is subjected to the constraints described in Table 2. The (c) V_S and (d) V_P/V_S models that result from an inversion where V_P/V_S values are allowed to range between 1.5 and 2.0 in the crystalline crust and the crust is isotropic. There is a strong trade-off between crustal V_P/V_S and the strength of radial anisotropy in the crust, but $V_P/V_S < 1.7$ is considered physically implausible.

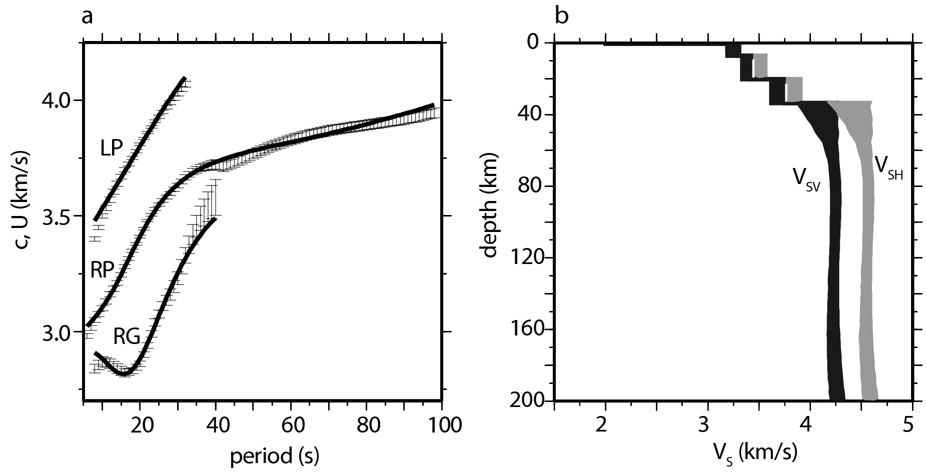

Figure 8. Inversion results from central Nevada (244.0,39.0). (a) Dispersion curve fit to the observed local dispersion values presented as error bars. The dispersion curves for the best-fitting model are plotted with solid black lines. (b) The corridor of accepted V_{SH} and V_{SV} models are plotted in light and dark gray, respectively. RP, RG, and LP refer to Rayleigh wave phase and group speed and Love wave phase speed, respectively.

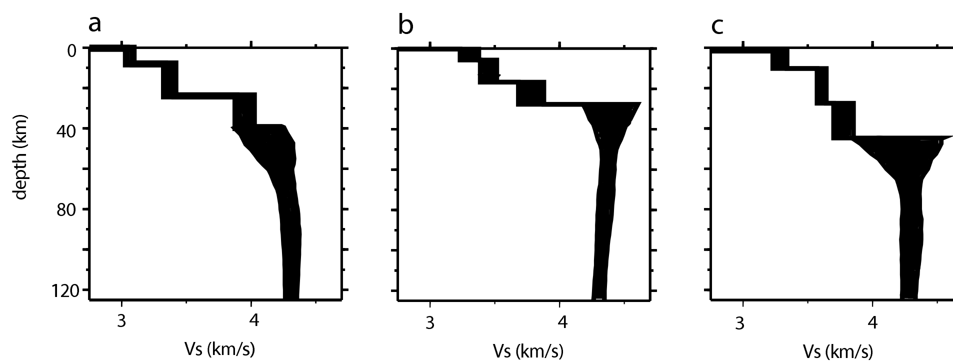

Figure 9. Examples of the isotropic V_S components of the radially anisotropic model m_1 for three different tectonic provinces. V_S models are presented for (a) the southern Cascadia Backarc (239.0,42.5), (b) the Yakima Fold Belt (241.0,47.0) and (c) the Colorado Plateau (248.0,38.0), identified by blue squares in Fig. 1.

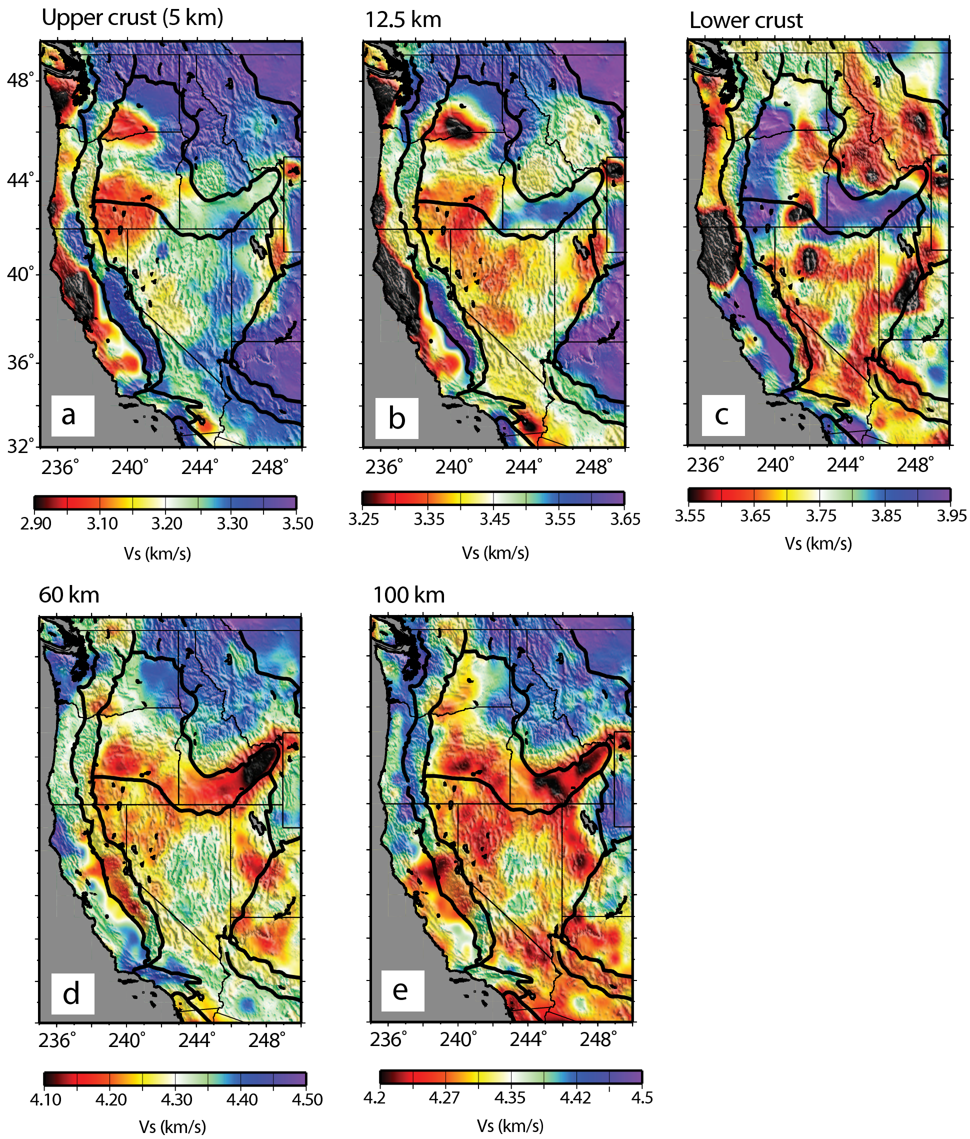

Figure 10. Depth slices through the western US in which V_S has been computed from the radially anisotropic model by Voigt averaging. The mean shear-velocities from the ensemble of accepted models are presented. Shear-velocities are plotted for the (a) upper crust, (b) 12.5 km depth, (c) lower crust, (d) 60 km depth, and (e) 100 km depth.

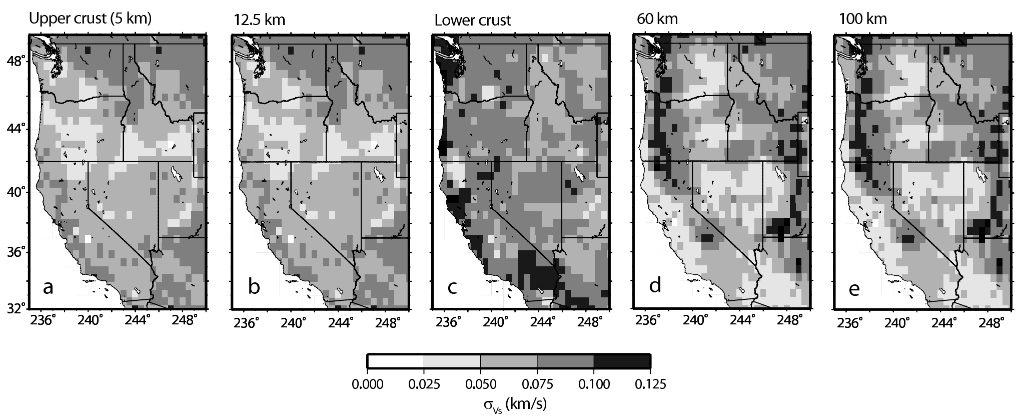

Figure 11. Uncertainty values associated with the shear-velocity estimates of Fig. 10 are plotted in absolute units for the (a) upper crust, (b) 12.5 km depth, (c) lower crust, (d) 60 km depth, and (e) 100 km depth. Uncertainties are defined as the standard deviation of the ensemble of accepted models at each depth.

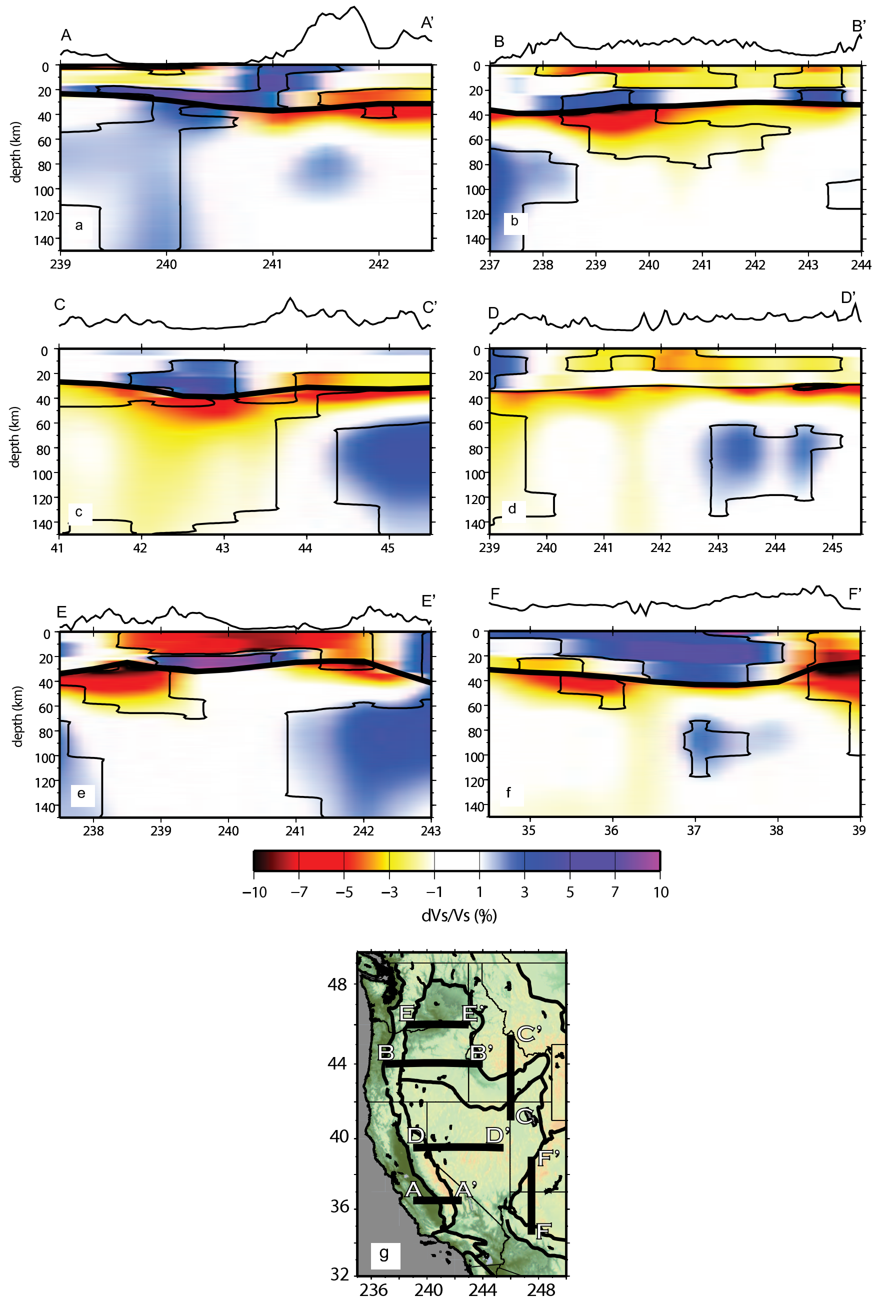

Figure 12. Vertical cross-sections through the western US V_S model. Velocities are plotted relative to the western US reference model presented in Fig. 12. Surface and Moho topography are plotted on each cross-section as black lines above and superimposed over the velocity anomaly plots, respectively. W-E cross-sections are plotted for latitudes (a) 36.5°, (b) 44.0°, (d) 39.5°, and (e) 46.0°. S-N cross-sections are plotted along longitudes (c) 246° and (f) 247.5°. Persistent features are outlined with black contours. The locations of the cross-sections in (a) – (f) are plotted and labeled in (g).

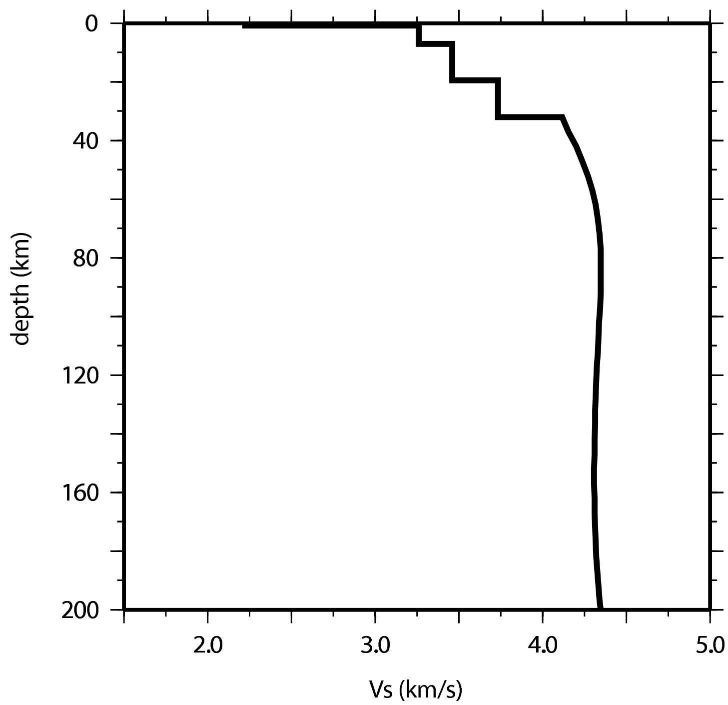

Figure 13. Western US average (reference) V_S model. The reference V_S model is constructed from the mean of all continental models in the western US. Crustal parameters are given in Table 2.

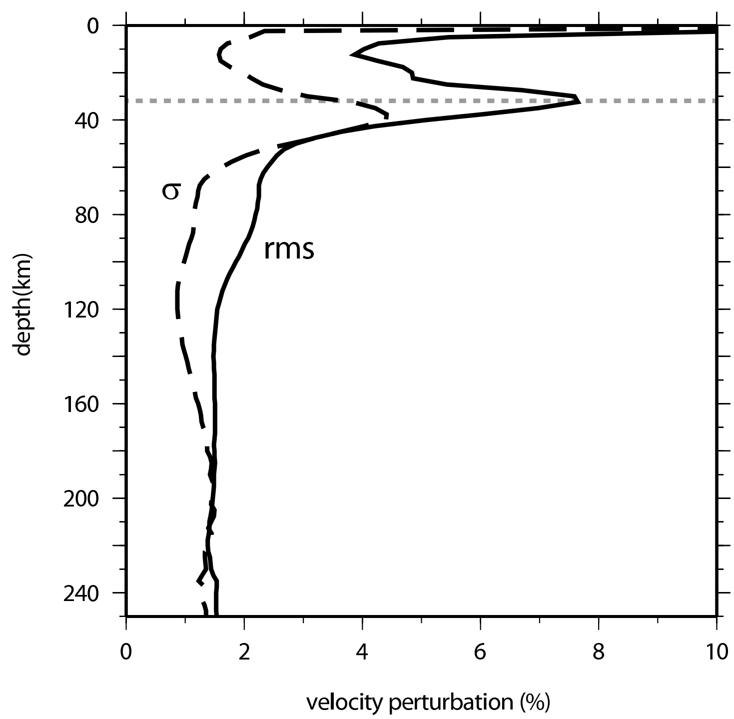

Figure 14. RMS lateral variation of the model and spatially average mean model uncertainty are plotted versus depth. Uncertainties are lowest in the middle crust and in the mantle at depths betwee about 60 and 150 km. RMS model anomalies are about twice the mean model uncertainty value, except between 30 – 55 km depth and below 110 km. Velocity trade-offs between the lower crust and mantle contribute to mean uncertainties greater than 2.5% from 30 – 45 km depth. The regionally-averaged Moho depth is plotted with a dashed gray line.

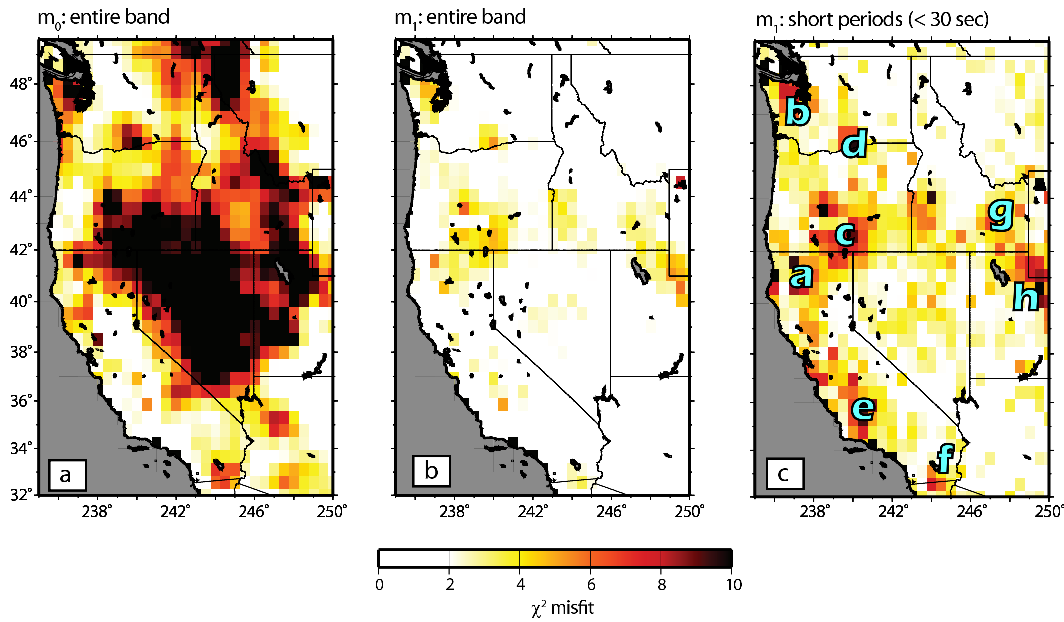

Figure 15. χ^2 values corresponding to the best-fitting isotropic (m_0) and radially anisotropic (m_1) V_S models across the entire period band and within the 6 – 30 sec period band for the radially anisotropic V_S model. (a) Entire band χ^2 values from the isotropic V_S model, m_0, show poor fit across large regions of the western US, particularly in extensional provinces such as the Basin and Range. The mean χ^2 value across the study region is 8.7. (b) Introduction of radial anisotropy to the crust and upper mantle in model m_1 reduces the regionally-averaged entire band χ^2 value to 2.4. (c) Short periodχ^2 values in the 6 – 30 sec period band for the radially anisotropic V_S model m_1. Short period dispersion measurements have strong sensitivity to the crust; thus, we refer to this plot as the "crustal misfit". Regions of poor short period fit include the Olympic Peninsula, Mendocino Triple Junction, southern Cascadia backarc, Yakima Fold Belt, Salton Trough, Snake River Plain, California Great Valley, Wasatch Range, and Yellowstone. The letter labels in panel (c) are also used in Fig. 16.

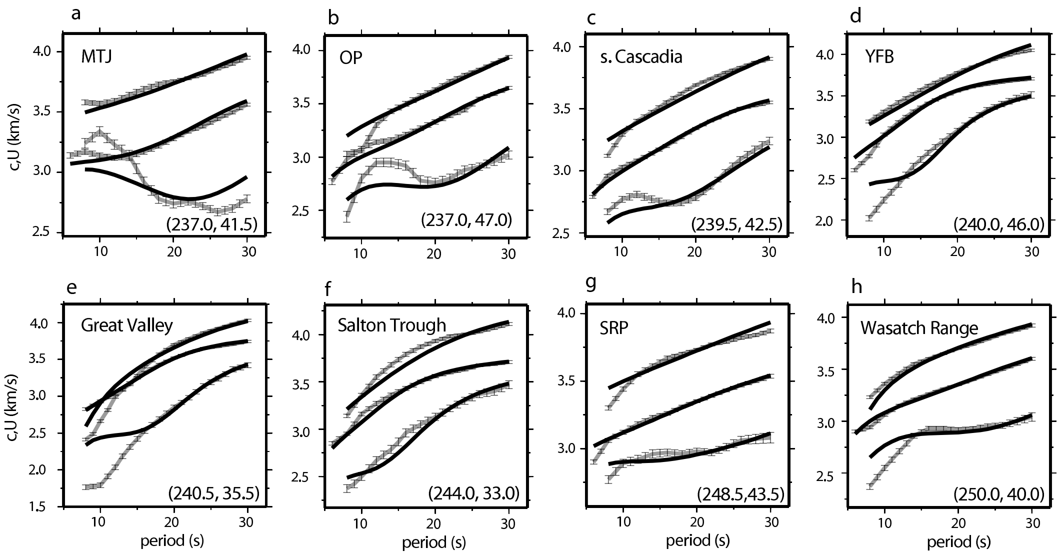

Figure 16. Characteristic short period dispersion curve misfits from the radially anisotropic V_S model. The best-fitting dispersion curves are plotted in black. Local dispersion curves and uncertainties are plotted with error bars and gray curves. Grid point inversion examples from the following regions in the western US are presented: (a) Mendocino Triple Junction (MTJ), (b) Olympic Peninsula (OP), (c) southern Cascadia backarc, (d) Yakima Fold Belt (YFB), (e) Great Valley, (f) Salton Trough, (g) Snake River Plain (SRP), and (h) Wasatch Range. The locations of the these inversions are identified with the corresponding letters in Fig. 15(c).